Remote sensing of complex permittivity and penetration depth of soils using P-band SAR polarimetry

Anke Fluhrer, Thomas Jagdhuber, Alireza Tabatabaeenejad, Seyed Hamed Alemohammad, Carsten Montzka, Peter Friedl, Ehsan Forootan, Harald Kunstmann

Angaben zur Veröffentlichung / Publication details:

Fluhrer, Anke, Thomas Jagdhuber, Alireza Tabatabaeenejad, Seyed Hamed Alemohammad, Carsten Montzka, Peter Friedl, Ehsan Forootan, and Harald Kunstmann. 2022. "Remote sensing of complex permittivity and penetration depth of soils using P-band SAR polarimetry." *Remote Sensing* 14 (12): 2755. https://doi.org/10.3390/rs14122755.

remote sensing

Article

Remote Sensing of Complex Permittivity and Penetration Depth of Soils Using P-Band SAR Polarimetry

Anke Fluhrer [1,2,*], Thomas Jagdhuber [1,2], Alireza Tabatabaeenejad [3], Hamed Alemohammad [4], Carsten Montzka [5], Peter Friedl [6], Ehsan Forootan [7] and Harald Kunstmann [2,8]

[1] Microwaves and Radar Institute, German Aerospace Center (DLR), Muenchenerstraße 20, 82234 Weßling, Germany; thomas.jagdhuber@dlr.de
[2] Institute of Geography, Augsburg University, Alter Postweg 118, 86159 Augsburg, Germany; harald.kunstmann@kit.edu
[3] The Aerospace Corporation, El Segundo, CA 90245, USA; alirezat@aero.org
[4] Radiant Earth Foundation, Washington, DC 20005, USA; h.alemohammad@gmail.com
[5] Institute of Bio- and Geosciences: Agrosphere (IBG-3), Forschungszentrum Jülich, Wilhelm-Johnen-Straße, 52428 Jülich, Germany; c.montzka@fz-juelich.de
[6] Earth Observation Center, German Aerospace Center (DLR), Muenchenerstraße 20, 82234 Weßling, Germany; peter.friedl@dlr.de
[7] Geodesy Group, Department of Planning, Aalborg University, Rendsburggade 14, 9000 Aalborg, Denmark; efo@plan.aau.dk
[8] Institute of Meteorology and Climate Research, Karlsruhe Institute of Technology, Kreuzeckbahnstraße 19, 82467 Garmisch-Partenkirchen, Germany
* Correspondence: anke.fluhrer@dlr.de; Tel.: +49-8153-28-3908

Citation: Fluhrer, A.; Jagdhuber, T.; Tabatabaeenejad, A.; Alemohammad, H.; Montzka, C.; Friedl, P.; Forootan, E.; Kunstmann, H. Remote Sensing of Complex Permittivity and Penetration Depth of Soils Using P-Band SAR Polarimetry. *Remote Sens.* **2022**, *14*, 2755. https://doi.org/10.3390/rs14122755

Academic Editor: Frédérique Seyler

Received: 4 May 2022
Accepted: 6 June 2022
Published: 8 June 2022

Abstract: A P-band SAR moisture estimation method is introduced for complex soil permittivity and penetration depth estimation using fully polarimetric P-band SAR signals. This method combines eigen- and model-based decomposition techniques for separation of the total backscattering signal into three scattering components (soil, dihedral, and volume). The incorporation of a soil scattering model allows for the first time the estimation of complex soil permittivity and permittivity-based penetration depth. The proposed method needs no prior assumptions on land cover characteristics and is applicable to a variety of vegetation types. The technique is demonstrated for airborne P-band SAR measurements acquired during the AirMOSS campaign (2012–2015). The estimated complex permittivity agrees well with climate and soil conditions at different monitoring sites. Based on frequency and permittivity, P-band penetration depths vary from 5 cm to 35 cm. This value range is in accordance with previous studies in the literature. Comparison of the results is challenging due to the sparsity of vertical soil in situ sampling. It was found that the disagreement between in situ measurements and SAR-based estimates originates from the discrepancy between the in situ measuring depth of the top-soil layer (0–5 cm) and the median penetration depth of the P-band waves (24.5–27 cm).

Keywords: AirMOSS; polarimetric decomposition; soil moisture; multi-layer SPM

1. Introduction

Soil moisture is one of the essential climate variables (ECVs) [1] "that critically contribute [. . .] to the characterization of [the] Earth's climate" [2] and its changes. Hence, it plays a crucial role within the hydrological and biogeochemical cycles [1,3–7]. Many approaches exist to retrieve soil moisture from air- or space-borne remote sensing observations, taking advantage of the sensitivity of active (radar) and/or passive (radiometer) microwave signals to soil moisture [8–12]. These studies allow an estimation of soil moisture predominantly from L-band measurements: on the one hand, because of the larger penetration capabilities compared to higher frequency bands, such as C- or X-band, and on the other hand, due to the availability of global L-band satellite data, e.g., from Soil

Moisture and Ocean Salinity (SMOS) (since 2009) [10] or Soil Moisture Active Passive (SMAP) (since 2015) [8] missions. Lower frequency bands such as P-band have only rarely been used to estimate soil moisture from space, mainly due to the lack of sensors operating at P-band frequencies. Nevertheless, with the European Space Agency (ESA) BIOMASS mission in 2023, the first P-band sensor in space will be launched [13]. In addition, the first on-orbit demonstration of the remote sensing technique will be started by the National Aeronautics and Space Administration (NASA) SigNals of Opportunity: P-band Investigation (SNoOPI) mission in 2022 [14,15]. Moreover, P-band airborne datasets, e.g., from the Airborne Microwave Observatory of Subcanopy and Subsurface (AirMOSS) campaign, are already available [16]. Hence, P-band data can also be employed for estimating soil moisture, e.g., by decomposing fully polarimetric radar signals into individual scattering mechanisms.

Incoherent decomposition theorems have been developed to decompose scattering from natural media and disentangle the different scattering contributions of the signal. Fully polarimetric synthetic aperture radar (PolSAR) provides measurements of the Earth's surface represented by a complex scattering matrix $[S]$, based on which the 3×3 covariance $[C]$ or coherence $[T]$ matrices can be calculated [9,17–19]. Among many decomposition methods, two basic categories can be distinguished: eigen-based, introduced by [20], or model-based, established by [21]. The first is based on the eigenvalue decomposition of the $[C]$ or $[T]$ matrix, leading to three parameters: the polarimetric entropy H, expressing the randomness of the polarimetric scattering process, the polarimetric anisotropy A, characterizing the secondary scattering processes, and the polarimetric scattering angle α, representing an intrinsic scattering mechanism [17,22,23].

The model-based decomposition simulates backscattering as the linear sum of multiple, mostly simple physical scattering mechanisms of canonical objects (e.g., spheres, dipoles) [18,22,24]. Here, $[C]$ or $[T]$ are decomposed into three components: surface, dihedral (double-bounce), and volume scattering. More detailed reviews of the decomposition theorems can be found in [25–30].

In order to take advantage of both, a combination of eigen- and model-based incoherent decomposition techniques was suggested by [24,31]. By including a generalized volume scattering model and under the assumption of scattering reflection symmetry ($\langle S_{HH}S_{HV}^{*}\rangle = 0$ & $\langle S_{VV}S_{HV}^{*}\rangle = 0$), an iterative hybrid decomposition method was proposed, combining eigen- and model-based techniques to decompose $[T]$ into the three canonical scattering components: surface $[T_s]$, dihedral $[T_d]$, and volume $[T_v]$ [24]. Assumed scattering reflection symmetry may only be violated significantly in urban or high mountain regions [27]. The authors of [24] demonstrated the feasibility of the proposed iterative hybrid decomposition method and the inversion algorithm for soil moisture estimation across various agricultural vegetation covers, based on L-band airborne SAR data of the operational discharge and flooding predictions in head catchments (OPAQUE), Synthetic Aperture Radar within TERENO framework (SARTEO), and AgriSAR campaigns from 2006 to 2008. Within this decomposition, two iterations to determine the appropriate initial permittivity and the best physically "constrained volume intensity component f_V" [24] are necessary. Although the results showed that the separation of volume scattering from ground scattering components is physically meaningful compared to in situ measurements, this iterative approach is complex in algorithmics, computationally expensive, and requires certain assumptions on initial conditions. Hence, [3] presented an adapted hybrid decomposition technique by combining the model-based decomposition technique of [18,21] with the eigen-based decomposition technique, as proposed in [24,27]. By employing observations of the AirMOSS campaign, [3] were the first to apply the hybrid decomposition method on P-band SAR data across a wide range of vegetation covers (from grasslands to dense forests). Further, no assumptions on initial vegetation conditions are made in that study, since "[volume] scattering is modeled using a cloud of randomly-oriented dipoles" [3]. For the decomposition of the total backscattering signal into the three scattering components $[T_s]$, $[T_d]$, and $[T_v]$, the volume scattering intensity f_V is estimated from the cross-polarized signal directly [31] by fixing the vegetation representations to dipoles that are randomly distributed [3] (cf. Section 3.2). The authors of [19] further explored the proposed hybrid decomposition approach by comparing results based on L- and P-band SAR observations from the AirMOSS campaign. Both studies demonstrated the applicability of the hybrid decomposition technique to P-band data of various biomes. Thus, results for soil and dihedral scattering contributions proved the usability of such hybrid techniques for designing soil moisture retrieval algorithms using polarimetric low frequency observations [3,19]. However, the authors concluded that the approach can be further improved by considering more than just one vegetation representation [3]. In the end, one main disadvantage of decomposition approaches is the well-known problem of overestimating the volume scattering component due to "discrimination [problems] between vegetation and oriented buildings" [32], leading to negative powers (physically impossible) [9,22,27,33].

The change in direction of the electromagnetic wave when it enters a dielectric medium can be related to its relative electric permittivity ε_r [–], formerly also called the dielectric constant [34,35]. In this study, the relative permittivity of soil is denoted by ε_s, which is a complex number with a real $\varepsilon_s{}'$ and an imaginary part $\varepsilon_s{}''$. In most studies, only the real part of ε_s is considered and investigated, e.g., [24,31,36–38]. However, in general, soils are lossy media, where $\varepsilon_s{}''$ is of significant importance when describing the soil permittivity and, hence, is investigated in this study.

The advantage of microwave remote sensing is the ability of electromagnetic waves to penetrate through vegetation or into the soil. In general, the lower the frequency, the larger the penetration into the soil, e.g., [5,35,39,40]. However, the penetration ability of microwaves is more complex and depends on varying factors besides frequency, such as the sensor itself, as well as soil or vegetation cover characteristics (e.g., incidence angle, polarization, soil texture, density, moisture, and surface roughness). Since the penetration depth is defined as depth after which the power density of the propagating electromagnetic radiation is reduced by a factor of $1/e$ ($\approx$0.37), e.g., [35,39,41], it is an important measure and indication in microwave remote sensing. For example, if the penetration depth is low, the contribution of the underlying soil to the backscattered waves is questionable and, hence, the signal may be insensitive to estimated soil moistures [42].

Dependent on ε_s, several more or less complex formulations to calculate the microwave penetration depth δ_p have been published, e.g., in [35,41,43–45]. Many of them depend mainly on the permittivity of the medium, the wavelength (frequency), and incidence angle of the incoming wave and, hence, do not account for scattering effects, system (e.g., sensitivity, calibration uncertainty), or medium (e.g., dielectric discontinuity) characteristics, but only attenuation effects of the medium [39]. Ref. [39] compared penetration depths at L-band (1.26 GHz) and P-band (430 MHz) frequencies across varying top-layer permittivities and concluded that δ_p "significantly underestimates the depths that radar backscatter can actually detect" [39]. One reason is that δ_p does not account for discrepancies between decreasing wave intensity with depth and the depth contribution to the total radar signal. However, in the case the radar signal-to-noise ratio is sufficiently high, variations beyond δ_p will be detected [46]. Furthermore, results showed smaller penetration capabilities of L-band frequencies compared to P-band [39]. Similarly, [40] determined the moisture retrieval depth from polarimetric L-band (1.400–1.426 GHz) and P-band (0.742–0.752 GHz) radiometer data, measured during the P-band Radiometer Inferred Soil Moisture (PRISM) project in 2019 at Core Lynn, Australia. The study was conducted to investigate the assumption of increasing moisture retrieval depths for longer wavelengths, and thus to show the potential of P-band wavelengths to retrieve soil moisture at larger depths than L-band. Their results overall confirmed that this assumption proves the potential of P-band measurements for subsurface soil moisture retrievals. However, the results also indicated that the moisture retrieval depth is not only dependent on frequency but also on the soil moisture gradient with depth, which diminishes the differences in retrieval depths of P- and L-band for higher moistures in the top soil layer [40]. Smaller penetration capabilities of L-band frequencies compared to P-band are also confirmed by the studies of [40,41,47], concluding that at P-band, influences of soil surface roughness and vegetation canopy are diminished. Nevertheless, numerical results from [48] revealed limited influence of small scale roughness on P-band backscatter simulations, but an increasing complexity between P-band signals and soil roughness at spatially larger scales.

In the literature, P-band is assumed to be able to estimate soil moisture across the root-zone of the soil (up to approx. 2 m depth) [5,49,50]. Consequently, a wide range of P-band penetration and sensing depths can be found in the literature, from some centimeters up to one meter or more [5,39,46,51]. Following the assumption that soil depths are accessible "in the order of one half to one tenth of the [employed] wavelength [52]" [45,47,53], P-band penetration depths of 6.97 to 34.86 cm at 430 MHz ($\lambda = 69.72$ cm) are potentially realistic. This value range was estimated, e.g., by [46] in a ten-year study based on P-band data near the Ameriflux site at Vaira Ranch, CA, USA. Additionally, within the AirMOSS P-band root-zone, soil moisture (RZSM) product sensing depths of typically 45 cm are considered [51]. Here, RZSM is estimated based on AirMOSS measurements together with simulations from a vegetation, surface, and subsurface scattering model by assuming a second-order polynomial function of the profile [54].

In this study, an adapted non-iterative hybrid P-band SAR decomposition method for moisture estimation is proposed to separate scattering mechanisms in fully polarimetric SAR data (Section 3.2). The proposed method utilizes a soil scattering model, which is suitable for P-band wavelengths (Section 3.1). The decomposition results are used in a consecutive step for the estimation of the complex permittivity, which in turn is applied for penetration depth calculations (Section 3.3). Thus, this study seeks to estimate complex permittivity from decomposed SAR signals and to determine permittivity-based P-band penetration capabilities to better understand P-band microwave behavior in soil along depth. For that, the proposed P-band SAR moisture estimation method continues the efforts of [3,24], and is the first of its kind, to the best of our knowledge, for complex soil permittivity estimation from (P-band) SAR data.

2. Materials

The polarimetric P-band SAR observations employed in this study were acquired during the AirMOSS campaign (a NASA Earth Venture-1 project) from 2012 to 2015 over nine different biomes across ten sites in Northern and Central America. This campaign was the first P-band airborne mission designed to estimate RZSM. The monitoring sites comprise varying land cover classes from bare soils to tropical rain forests. Each site covers an area of approximately 25 × 100 km at ~100 m spatial resolution and was revisited at least two to four times every year during the campaign. The P-band instrument operated at a center frequency of 430 MHz ($\lambda \approx 69.72$ cm). With a high radiometric calibration accuracy (0.5 dB) and a noise equivalent σ^o of -40 dB, the AirMOSS dataset provides P-band SAR measurements, which are very well suited for estimating soil and vegetation parameters [3]. Detailed information on the campaign can be found in, e.g., [3,16].

The AirMOSS dataset provides measurements for a total of 168 dates at ten sites, each of them covering an area of 25 × 100 km. Hence, in this study, only a subset of the dataset was processed and analyzed, with focus on the three AirMOSS monitoring sites "MOISST" in Oklahoma, "Walnut Gulch" in Arizona, and "Harvard Forest" in Massachusetts, USA. By choosing these three monitoring sites, varying vegetation types and climatic conditions are analyzed. Furthermore, every study area is filtered for pixels classified as water, snow, wetlands, developed ground, bare soil, and pasture/hay, as well as for incidence angles smaller than 30° and greater than 50°, to narrow down the amount of data to be processed and to focus on vegetated soils.

Lastly, only four dates per year and monitoring site are evaluated, in the case data for more than four dates are available (Figure 1). Walnut Gulch in Arizona is characterized by an arid to semi-arid climate of a hot desert (BWh), MOISST in Oklahoma by a temperate climate with hot summers (Cfa), and Harvard Forest in Massachusetts by a cold humid continental climate with warm summers (Dfb) [55].

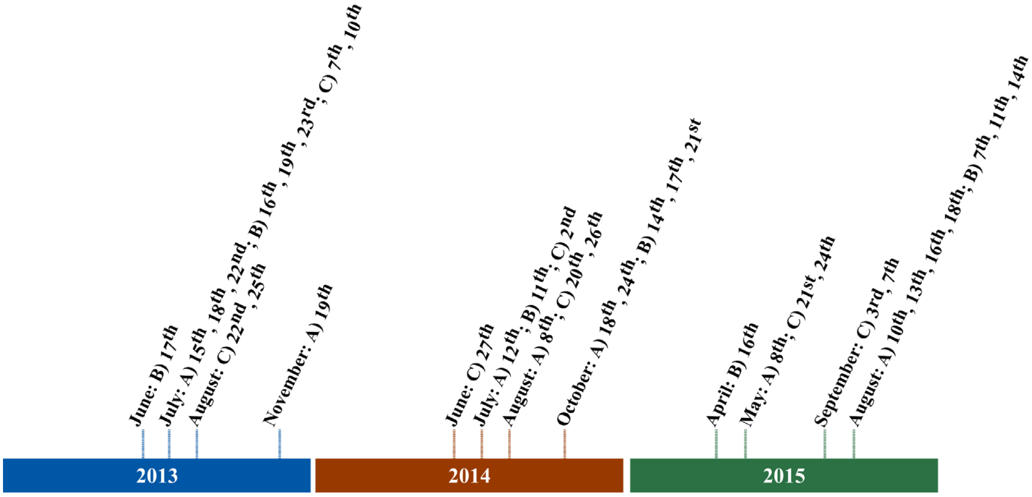

Figure 1. Timeline of processed AirMOSS dates per year and for every monitoring site. (A) Walnut Gulch, AZ, USA. (B) MOISST, OK, USA. (C) Harvard Forest, MA, USA.

In Figure 2, the land cover types according to the National Land Cover Database (NLCD) [56], as provided within the AirMOSS datasets, are shown for every monitoring site. The percentages in Table 1 represent the respective number of pixels per land cover class in comparison to all processed pixels (after filtering). Walnut Gulch (Figure 2A) is mostly covered by shrub/scrub (92.5%) while other classes represent less than 5% of all pixels (Table 1). The monitoring site MOISST (Figure 2B) is mainly covered by grassland/herbaceous (51.5%) and cultivated crops (38.3%), while Harvard Forest (Figure 2C) is covered by deciduous (49%), mixed (30.4%), and evergreen (25.1%) forests (Table 1).

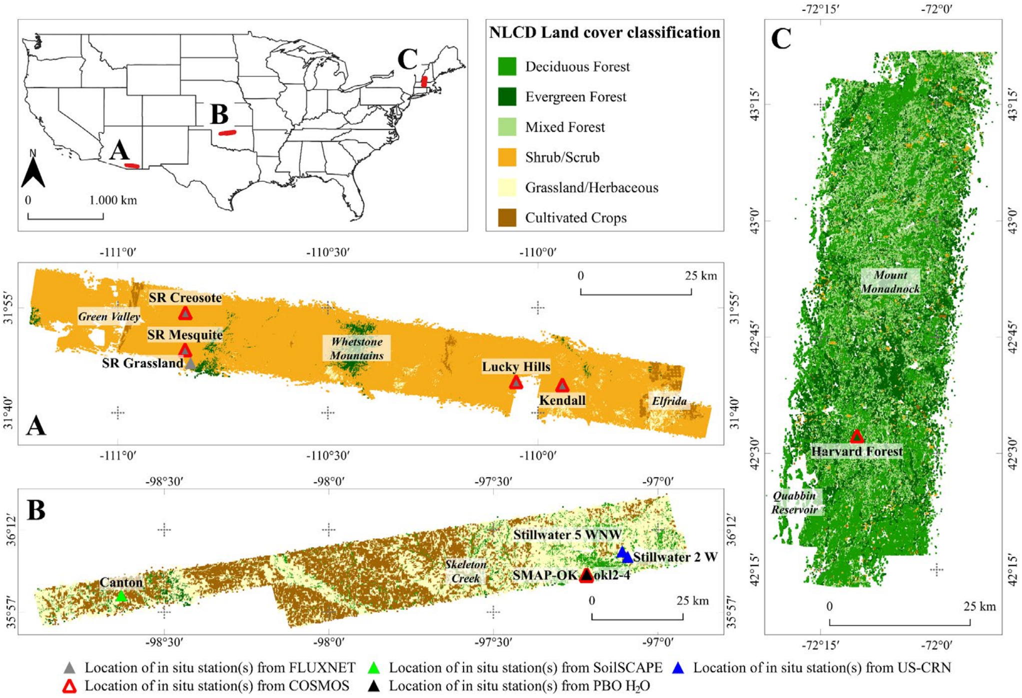

Figure 2. Overview of NLCD land cover classifications at the study areas of individual AirMOSS monitoring sites in the US with locations (triangles) of in situ measurement stations from various networks. (**A**) Walnut Gulch, AZ, USA. (**B**) MOISST, OK, USA. (**C**) Harvard Forest, MA, USA. Political state boundaries of the U.S. are from https://hifld-geoplatform.opendata.arcgis.com/.

Table 1. Distribution of NLCD land cover classes at every AirMOSS monitoring site (%) (in relation to the total of all processed pixels after filtering).

NLCD Land Cover Class	**AirMOSS Monitoring Site**		
	Walnut Gulch	**MOISST**	**Harvard Forest**
Grassland/herbaceous	2.2	51.5	0.3
Shrub/scrub	92.5	0	1.8
Cultivated crops	2.2	38.3	0.3
Deciduous forest	<0.1	8.3	49
Evergreen forest	3	1.7	25.1
Mixed forest	<0.1	0.3	30.4

For a later comparison of SAR-based estimates, the daily averages of in situ soil moisture measurements from five different networks at 17 stations are used as shown in Figure 2. At Walnut Gulch, five stations from the FLUXNET2015 dataset [57] and four stations from the Cosmic-ray Soil Moisture Observing System (COSMOS) [58,59] are employed. At MOISST, one station from the Soil moisture Sensing Controller And oPtimal Estimator (SoilSCAPE) project [60], and COSMOS, two stations from the US Climate Reference Network (US-CRN) [61], and three stations from the Plate Boundary Observatory to study the water cycle (PBO H_2O) project [62] are used. Lastly, at Harvard Forest, one station from COSMOS is employed (Figure 2).

3. Methods

In this study, the proposed P-band SAR moisture estimation method consists of a hybrid decomposition method and a subsequent moisture estimation procedure. The hybrid decomposition method combines eigen- and model-based decomposition techniques to separate P-band SAR signals into individual scattering mechanisms. For the determination of the scattering components, the method is supported by a soil scattering model, the first-order multi-layer small perturbation method (SPM) [63]. Subsequently, based on the decomposed scattering components, the complex soil permittivity is estimated. The individual processing steps of the method are shown in Figure 3 and explained in detail in the following.

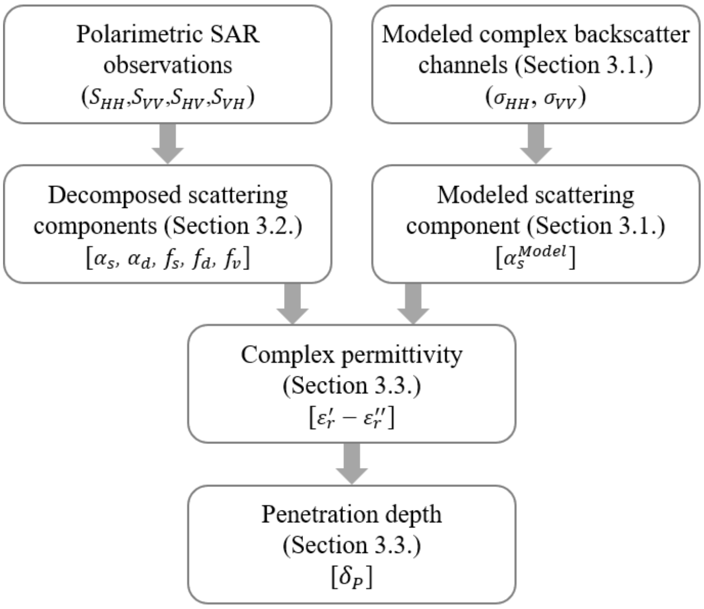

Figure 3. Flow chart of the proposed P-band SAR moisture estimation method for complex soil permittivity and penetration depth estimation based on decomposed scattering components.

3.1. Soil Scattering Based on Multi-Layer SPM

The first-order multi-layer SPM [63] is employed to model the scattering angle α_s^{Model}, needed within the proposed hybrid decomposition method (cf. Section 3.2).

As shown on the right side of Figure 3, modeled complex backscatter channels, denoted by σ_{pp} [–] for horizontal or vertical polarization, are required to estimate the model-based α_s^{Model}. In this study, σ_{pp} are modeled with the first-order solution of the multi-layer SPM [63], which computes backscatter coefficients based on soil characteristics for multiple soil layers with depth. The ability of this model to consider backscattering from multiple subsurface layers qualifies it to be more suitable for analyzing P-band soil interactions than a soil surface-only scattering model such as the SPM, also called Bragg model [27,64], as shown in [63]. The multi-layer SPM computes first-order scattering from layered surfaces by considering “multiple scattering processes between the boundaries” [63]. Since the model was originally designed to compute backscattering coefficients σ_{pp}^o, it was adapted in order to simulate complex backscatter channels σ_{pp}, where $\sigma_{pp}^o = |\sigma_{pp}|^2$ holds. The complex backscatter channels σ_{pp} are estimated by:

$$\sigma_{pp} = \sqrt{4\pi k_0^2 cos^2\theta_s \xi^2 * \left(\begin{array}{c} \left(\alpha_{pp}^{f_1}\left(k_\perp^s\right) * \alpha_{pp}^{f_1^*}\left(k_\perp^s\right)\right) W_{f_1}\left(k_\perp^s - k_\perp^i\right) + 2\Re\left\{\alpha_{pp}^{f_1}\left(k_\perp^s\right)\alpha_{pp}^{f_2^*}\left(k_\perp^s\right)\right\} * \\ W_{f_1 f_2}\left(k_\perp^s - k_\perp^i\right) + \left(\alpha_{pp}^{f_2}\left(k_\perp^s\right) * \alpha_{pp}^{f_2^*}\left(k_\perp^s\right)\right) * W_{f_2}\left(k_\perp^s - k_\perp^i\right) \end{array} \right)} \tag{1}$$

with $\alpha_{pp}^{f_1}\left(k_\perp^s\right)$ and $\alpha_{pp}^{f_2}\left(k_\perp^s\right)$ as coefficients related to the incident field, $W_{f_1}\left(k_\perp\right)$ and $W_{f_2}\left(k_\perp\right)$ as the power spectral densities of the rough boundaries, and with $W_{f_1 f_2}\left(k_\perp\right)$ as their joint spectral density [63]. In detail, if the incident electric field is p-polarized, the first-order p-polarized scattered electric field in the direction k^s is a linear function of the Fourier transforms of the rough boundary functions f_1 and f_2, with the corresponding coefficients denoted by $\alpha_{pp}^{f_1}\left(k_\perp^s\right)$ and $\alpha_{pp}^{f_2}\left(k_\perp^s\right)$. Lastly, the square root of a complex number is calculated according to Moivre’s theorem [65]. The reader is referred to [63] for detailed information on backscatter coefficient calculations.

In Table 2, the required input parameters of the multi-layer SPM for simulating σ_{pp} are listed together with their respective values used in this study. Please note that the chosen values are one possible approximation for the acquisition scenario in this study and may need to be adapted for different scenarios and other studies.

Table 2. Required input parameters of the multi-layer SPM for σ_{pp} simulations with the applied values in this study.

Parameter	Value
Frequency, f [MHz]	430
Number of layers, N [–]	2
Incidence angle in range, θ_i, and azimuth, φ_i [°]	θ_i from AirMOSS; $\varphi_i = 0$
Scattering angle in range θ_s, and azimuth, φ_s [°]	$\theta_s = \theta_i$; $\varphi_s = 180$
z-coordinates of the respective boundary layer, d_1 [cm]	$d_1 = \lambda/2 = 34.86$
Surface roughness parameters of each layer [cm] (vertical RMS height s, horizontal correlation length l)	s_1, l_1, s_2, and l_2 are dependent on roughness indicator derived from TanDEM-X (Table 3, right column)
Autocorrelation function, ACF [–]	Exponential
Complex permittivity $\varepsilon_s = \varepsilon_s' - j\varepsilon_s''$ of each layer [–]	$\varepsilon_{s_1}: \varepsilon_s' \in [6, 40]$, $\varepsilon_s'' \in [0, 10]$ $\varepsilon_{s_2} = \varepsilon_{s_1} + (10 + j0.5)$

Table 3. Surface roughness parameter sets of each layer (vertical RMS height s, horizontal correlation length l) as input for the multi-layer SPM based on TanDEM-X derived roughness indicator R_{TDX}.

Roughness Indicator from TanDEM-X [m]	Input Roughness Parameters [cm]
$R_{TDX} < 5$	$s_1 = 0.5; l_1 = 30; s_2 = 0.25; l_2 = 60$
$5 \leq R_{TDX} < 10$	$s_1 = 1.5; l_1 = 25; s_2 = 0.75; l_2 = 50$
$10 \leq R_{TDX} < 15$	$s_1 = 2; l_1 = 20; s_2 = 1; l_2 = 40$
$R_{TDX} \geq 15$	$s_1 = 3; l_1 = 15; s_2 = 1.5; l_2 = 30$

Following findings by [48] (cf. Section 1), the surface roughness parameters, required for modeling P-band backscatter channels, are not fixed to static values in this study. However, since no information on surface roughness is available for AirMOSS monitoring sites with comparable spatial resolution, the DLR TanDEM-X DEM at 90 m resolution [66], downloadable at https://download.geoservice.dlr.de/TDM90/ (accessed on 5 March 2021), is used to derive a first-order roughness indicator for each site. For this, TanDEM-X elevations were resampled to the AirMOSS resolution, converted to roughness values with the GDAL DEM utility algorithm [67] in QGIS© [68], and scaled according to the employed wavelength ($\lambda = 69.72$ cm). The resulting roughness values, giving the degree of irregularity of the surface, serve as roughness indicators in this study. Hence, depending on this roughness indicator R_{TDX} (Table 3, left column), typical surface roughness parameter sets for each layer (Table 3, right column) were fixed as model input to account for varying roughness during simulations (from smooth to rather rough). It can be seen that the chosen values for vertical RMS height s vary from 0.25 to 3 cm, and for horizontal correlation length l from 15 to 60 cm. These values were fixed based on several sensitivity analyses and after reviewing the literature.

Lastly, complex backscatter channels σ_{pp}, for respective horizontal and vertical polarization, are used to calculate α_s^{Model}. In this study, the formulation by [27] is used, valid for $0 \leq \alpha_s \leq \frac{\pi}{2}$:

$$\alpha_s^{Model} = tan^{-1}\left(\frac{\sigma_{HH} - \sigma_{VV}}{\sigma_{HH} + \sigma_{VV}}\right). \tag{2}$$

In this study, α_s^{Model} is calculated for realistic ranges of complex soil permittivity ε_s [–] (real part: $\varepsilon_s' \in [6, 40]$, imaginary part: $\varepsilon_s'' \in [0, 10]$, with $0.1 < \varepsilon_s'' / \varepsilon_s' < 0.5$).

3.2. Polarimetric Hybrid Decomposition Method

The hybrid decomposition method was originally introduced by [24] as an iterative approach (cf. Section 1) specifically designed for L-band data. However, it is adapted here to be applied in a non-iterative way to P-band observations, and for estimating complex permittivity. As illustrated in Figure 3, the hybrid decomposition method separates polarimetric SAR observations into individual scattering components (surface, dihedral, and volume).

First, the polarimetric coherency $[T]$ matrix is defined as:

$$[T] = \begin{bmatrix} T_{11} & T_{12} & 0 \\ T_{12}^* & T_{22} & 0 \\ 0 & 0 & T_{33} \end{bmatrix} \tag{3}$$

with T_{12}^* as complex conjugate. By assuming reflection symmetry of the observed media, the correlation terms between co- and cross-polarized signals are zero (T_{13}, T_{23}, T_{31}, and T_{32}). Reflection symmetry can be assumed for one, because the correlation terms that are set to zero (due to reflection symmetry) are neither important for the decomposition, nor for the soil permittivity estimation. Second, areas where this symmetry may be violated, such as urban or high mountain regions, are not considered during the analyses (cf. Section 2) [27].

$[T]$ can be decomposed into the three canonical scattering components of surface $[T_s]$, dihedral $[T_d]$, and volume $[T_v]$:

$$\begin{bmatrix} T_{11} & T_{12} & 0 \\ T_{12}^* & T_{22} & 0 \\ 0 & 0 & T_{33} \end{bmatrix} = [T_s] + [T_d] + [T_v]. \tag{4}$$

The rank-3, model-based vegetation volume component $[T_v]$ is described by:

$$[T_v] = \frac{f_v}{2 + 2A_p^2} \begin{bmatrix} V_{11} & V_{12} & 0 \\ V_{12}^* & V_{22} & 0 \\ 0 & 0 & V_{33} \end{bmatrix} \tag{5}$$

with f_v as volume scattering intensity, and A_p [–] as particle anisotropy, which describes the shape of vegetation volume scatterers from vertical dipoles ($A_p = 0$) and spheres ($A_p = 1$) to horizontal dipoles ($A_p = \infty$). f_v is given by:

$$f_v = \frac{4V_{12} cos(2\alpha_s)\left(T_{12}^* - T_{12} + \left(T_{12} + T_{12}^*\right) cos(2\alpha_s)\right) + (T_{11} - T_{22})(V_{11} - V_{22})(cos(4\alpha_s) - 1) - \sqrt{RT}}{4V_{12}^2 - V_{11}^2 + 2V_{11}V_{12} - V_{22}^2 + \left(4V_{12}^2 + (V_{11} - V_{22})^2\right) cos(4\alpha_s)} \tag{6}$$

with $RT = \left|\left(2\left(T_{12} - T_{12}^*\right)(V_{11} - V_{22}) sin(2\alpha_s) + \left(2(T_{11} - T_{22})V_{12} - \left(T_{12} + T_{12}^*\right)(V_{11} - V_{22})\right) sin(4\alpha_s)\right)^2\right|$, and the polarimetric scattering angle α_s as model-based α_s^{Model} [24,31] (cf. Section 3.1). Further, the parameters for estimating the vegetation volume component are given by:

$$V_{11} = \left(A_p + 1\right)^2, \tag{7}$$

$$V_{12} = \left(A_p^2 - 1\right) sinc(2\Delta\psi), \tag{8}$$

$$V_{22} = \frac{1}{2}\left(A_p - 1\right)^2 (1 + sinc(4\Delta\psi)), \tag{9}$$

$$V_{33} = \frac{1}{2}\left(A_p - 1\right)^2 (1 - sinc(4\Delta\psi)), \tag{10}$$

with $\Delta\psi$ [°] as width of the orientation angle distribution, which describes the degree of orientation of the vegetation volume from oriented ($\Delta\psi = 0°$) to random ($\Delta\psi = 90°$).

Hence, (4) can be rearranged together with (5) in order to determine the soil parameters from the individual soil scattering components ($[T_s]$, $[T_d]$), by subtracting the volume component:

$$[T_s] + [T_d] = \begin{bmatrix} T_{11} & T_{12} & 0 \\ T_{12}^* & T_{22} & 0 \\ 0 & 0 & T_{33} \end{bmatrix} - \frac{f_v}{2 + 2A_p^2} \begin{bmatrix} V_{11} & V_{12} & 0 \\ V_{12}^* & V_{22} & 0 \\ 0 & 0 & V_{33} \end{bmatrix}. \tag{11}$$

As already mentioned, [24] originally proposed an iterative estimation procedure to find the most suited volume descriptions, namely f_v, A_p, and $\Delta\psi$. However, since this approach is computationally expensive and needs certain assumptions (bare soil regions in the observation area) to be initialized, a non-iterative way for estimating f_v is proposed here, independent of bare areas, by employing the model-based α_s^{Model} and a realistic parameter space for vegetation volume parameters, with $Ap \in [0, 1]$ and $\Delta\psi \in [0°, 90°]$.

Thus, together with α_s^{Model}, the SAR measurements are decomposed into the two eigen-based scattering angles α_s and α_d [°], as well as the scattering intensities of surface f_s, dihedral f_d, and volume f_v [–] for multiple $Ap - \Delta\psi$ combinations. The ability of the method to estimate five variables (α_s, α_d, f_s, f_d, and f_v) out of four SAR observations ($|S_{HH}|^2$, $|S_{VV}|^2$, $|S_{HV}|^2$, $|S_{VH}|^2$) is possible, since the ambiguity for α_s and α_d is solved by assuming an orthogonality condition with $\alpha_s = \pi/2 - \alpha_d$ [27], meaning, if the decomposed polarimetric scattering angle α is smaller than or equal to 45°, surface scattering is assumed, denoted by α_s, whereas in the case α is greater than 45°, dihedral scattering is assumed, denoted by α_d [24]. This way, in contrast to model-based-only approaches, the proposed method needs no prior assumptions on vegetation characteristics, and provides the advantage of incorporating actual SAR measurements.

The surface $[T_s]$ and dihedral $[T_d]$ scattering components are defined in (12) and (13), respectively, assuming that both are orthogonal rank-1 components [3,24]:

$$[T_s] = f_s \begin{bmatrix} cos^2\alpha_s & -sin\alpha_s & 0 \\ -cos\alpha_s & sin^2\alpha_s & 0 \\ 0 & 0 & 0 \end{bmatrix}, \tag{12}$$

$$[T_d] = f_d \begin{bmatrix} sin^2\alpha_d & cos\alpha_d & 0 \\ sin\alpha_d & cos^2\alpha_d & 0 \\ 0 & 0 & 0 \end{bmatrix}. \tag{13}$$

Finally, (11) can be reformulated to:

$$\begin{bmatrix} T_{11} & T_{12} & 0 \\ T_{12}^* & T_{22} & 0 \\ 0 & 0 & T_{33} \end{bmatrix} - f_v \begin{bmatrix} V_{11} & V_{12} & 0 \\ V_{12}^* & V_{22} & 0 \\ 0 & 0 & V_{33} \end{bmatrix} = \begin{bmatrix} f_s cos^2\alpha_s + f_d sin^2\alpha_d & (f_d - f_s)cos\alpha_{d,s} sin\alpha_{d,s} & 0 \\ (f_d - f_s)cos\alpha_{d,s} sin\alpha_{d,s} & f_d cos^2\alpha_d + f_s sin^2\alpha_s & 0 \\ 0 & 0 & 0 \end{bmatrix} \tag{14}$$

with the surface scattering intensities given by [24]:

$$\begin{aligned} & f_{s,d} \\ & = \tfrac{1}{2}\,(T_{11} + T_{22} - f_v * (V_{11} + V_{22}) \\ & \pm \sqrt{\left| -4\big(T_{22}(T_{11} - f_v T_{11}) + (T_{12} - f_v T_{12})\big(f_v V_{12} - T_{12}^*\big) + f_v(f_v V_{11} - T_{11})V_{22}\big) + (T_{11} + T_{22} - f_v * (V_{11} + V_{22}))^2 \right|}\,\Big) \end{aligned} \tag{15}$$

and the eigen-based scattering angle α to separate contributions from surface and dihedral scattering, given by [24]:

$$\alpha_{s,d} = acos\left(\left(1 + 4 * \left(\frac{T_{12}^* - f_v V_{12}}{T_{11} - T_{22} - f_v V_{11} + f_v V_{22} \pm \sqrt{RT}} \right)^2 \right)^{-\frac{1}{2}} \right) \tag{16}$$

with $RT = \left| T_{11}^2 + (T_{22} + f_v V_{11})^2 + 4(T_{12} - f_v V_{12})(T_{12}^* - f_v V_{12}) - 2T_{11}(T_{22} + f_v(V_{11} - V_{22})) - 2f_v(T_{22} + f_v V_{11})V_{22} + f_v^2 V_{22}^2 \right|$.

In summary, from polarimetric SAR observations and simulated α_s^{Model}, the decomposition results for α_s, α_d, f_s, f_d, and f_v can be estimated for varying ε_s and individual $Ap - \Delta\psi$ combinations. Hence, the proposed method overcomes the computationally expensive iterative procedure as proposed in [24], and provides the possibility of including multiple vegetation characteristics (Ap, $\Delta\psi$) as suggested by [3] (cf. Section 1). In this study, not all $Ap - \Delta\psi$ combinations are applied. Firstly, to ensure non-negative decomposed powers, scattering intensities for any $Ap - \Delta\psi$ combination that are smaller than zero are eliminated for subsequent analyses in order to avoid possible overestimation of the volume scattering component (cf. Section 1.). Secondly, the radar vegetation index (RVI) is used to exclude unrealistic $Ap - \Delta\psi$ combinations. Here, the RVI_{model} is modeled according to [31,69] for all $Ap - \Delta\psi$ combinations used within the approach. Afterwards, the data-based RVI_{data} is calculated for every pixel based on the respective SAR backscatter observations. Finally, all $Ap - \Delta\psi$ combinations, where the RVI_{model} deviates from RVI_{data} around the average value ($\overline{RVI_{model}}$) of all RVI_{model} ($RVI_{model} \notin RVI_{data} \pm \overline{RVI_{model}}$), are excluded from further analyses.

3.3. Complex Permittivity Estimation

The P-band SAR moisture estimation method proposed in this study provides the advantage of complex permittivity estimation. The real part of the permittivity $\varepsilon_s{}'$ is associated with energy or heat storage, and the imaginary part of the permittivity $\varepsilon_s{}''$

is associated with energy or heat loss, often called dielectric loss factor [35,70]. Since model-based α_s^{Model} is used to estimate f_v during the decomposition of polarimetric SAR observations, decomposition results can be calculated for a realistic range of soil permittivity values. Subsequently, by determining the closest fit between decomposed data-based α_s^{Data} and model-based α_s^{Model} for individual $Ap - \Delta\psi$ combinations (cf. Section 3.2.), the corresponding ε_s value can be estimated.

For that, the absolute value of the modulus r [–] and phase angle ϕ [–] of the real (α_s') and imaginary (α_s'') parts of α_s^{Data} and α_s^{Model}, respectively, are calculated:

$$r_{\alpha_s}(\varepsilon_s,\ Ap, \Delta\psi) = \left|\sqrt{\alpha_s'^2 + \alpha_s''^2}\right|, \tag{17}$$

$$\phi_{\alpha_s}(\varepsilon_s,\ Ap, \Delta\psi) = \left|tan^{-1}\left(\frac{\alpha_s''}{\alpha_s'}\right)\right|. \tag{18}$$

Afterwards, the smallest sum of the absolute differences between data- and model-based r_{α_s} and ϕ_{α_s} is used to determine ε_s:

$$\varepsilon_s(Ap, \Delta\psi) = argmin\left(\left|r_{\alpha_s^{Data}} - r_{\alpha_s^{Model}}\right| + \left|\phi_{\alpha_s^{Data}} - \phi_{\alpha_s^{Model}}\right|\right). \tag{19}$$

Since complex ε_s are estimated for multiple $Ap - \Delta\psi$ combinations to cover realistic vegetation volume characteristics (cf. Section 3.2), the final complex ε_s is the average value of $\varepsilon_s(Ap, \Delta\psi)$ for all remaining realistic $Ap - \Delta\psi$ combinations (non-negative surface scattering powers, modeled RVI_{model} around data-based RVI_{data}) (cf. Section 3.2).

For comparison, permittivity can be converted to soil moisture and vice versa, by employing dielectric mixing models, such as the one by Topp et al., [71], Dobson et al., [72], or Mironov et al., [73]. An extended review of dielectric mixing models for soils can be found in [74]. In this study, ε_s' results are converted to soil moisture θ [vol.%] according to the dielectric mixing model of [71].

Based on estimated complex ε_s from decomposed polarimetric SAR observations, one possible application is the estimation of the penetration depth δ_p [cm]. In this study, the well-known formulation of [75] is adapted to calculate δ_p [44]:

$$\delta_p = \frac{1}{2} * \left(\frac{\lambda}{2\pi} * \left[\frac{2}{\varepsilon_s' * \left(\sqrt{1 + tan^2(\varepsilon_s''/\varepsilon_s')} - 1\right)}\right]^{\frac{1}{2}}\right). \tag{20}$$

This formulation was chosen because almost all available equations to estimate δ_p are comparable and mainly dependent on the attenuation factor α, a measure for the penetration depth of an electromagnetic wave in a medium. However, this is one of the first to be published and well known.

Sensitivity studies and analyses with other published formulations for δ_p, e.g., [41,43,45,76], showed overall similar results ($R^2 > 0.99$) with small deviations ($\sigma < 5$ cm). In fact, deviations were only noticeable at very low permittivity.

Since δ_p is only dependent on complex permittivity and wavelength (frequency) (cf. Equation (20)), it is considered in this study as permittivity-based penetration depth to analyze potential depths for P-band signals. For a better understanding of how δ_p behaves across varying permittivity levels at P-band (430 MHz), modeling results are displayed in Figure 4. It can be seen that δ_p decreases with increasing permittivity, as expected. Further, δ_p estimates significantly decrease with increasing ε_s'', proving the importance of ε_s'' for δ_p calculations.

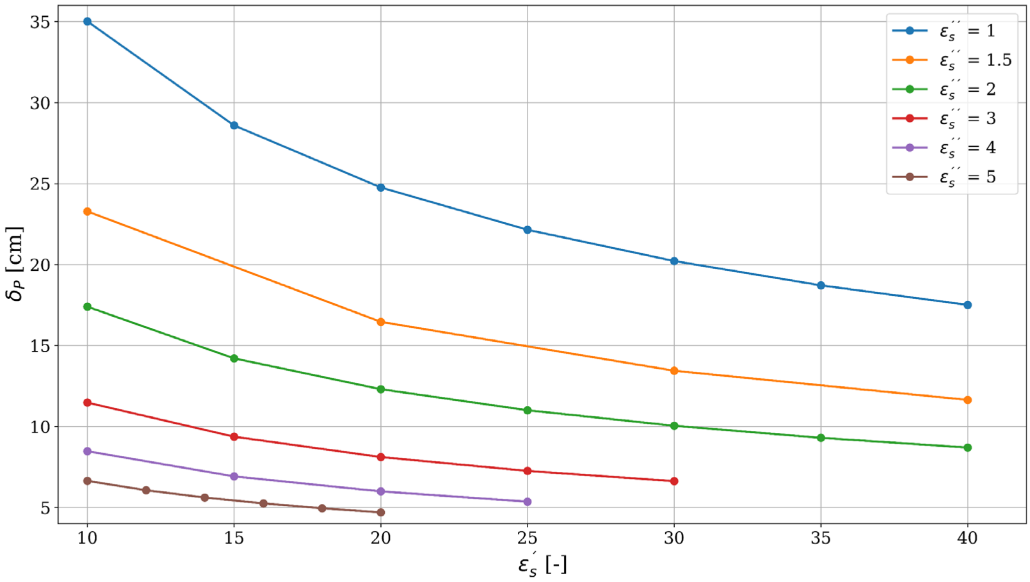

Figure 4. Variations in penetration depth estimates for P-band frequency (430 MHz) along varying real ε_s' and imaginary ε_s'' parts of complex permittivity based on the formulation from [44,75] (cf. Equation (20)).

4. Results

In this section, the results of the P-band SAR moisture estimation method are presented, comprising filtered and decomposed SAR signals, estimated complex permittivity, and soil moisture, as well as permittivity-based penetration depths. Furthermore, the results are related to in situ measurements from various networks (cf. Section 2) to compare the complex permittivity estimates.

4.1. Decomposition Results

Based on the proposed hybrid decomposition method, the relative indices P_s/P_t, P_d/P_t, and P_v/P_t for soil, dihedral, and volume are estimated to analyze the normalized contribution of each scattering mechanism. The indices are calculated based on the decomposition results for scattering angles and intensities according to [3].

In Figure 5, only the dominant scattering mechanisms, characterized by their relative indices, are shown for each AirMOSS monitoring site. Apparent data gaps (white areas in Figure 5) in the results originate from filtering for specific land cover classes and incidence angles prior to the processing (cf. Section 2). Here, brown regions represent dominant soil scattering, meaning the normalized contribution of soil scattering is the highest of all three contributions. Accordingly, beige regions represent dominant dihedral scattering, while dark green regions represent dominant volume scattering.

It can be seen that Walnut Gulch is mainly characterized by volume scattering, with dihedral scattering in the eastern part of the site, where cultivated crops are the main land cover class, as well as soil and dihedral scattering in the western part of the site near the *Green Valley* south of *Tucson* (Figure 2, Section 2). In this particular region, the influence of the incidence angle is evident since dominant volume scattering is mixed with dominant soil scattering, despite the same land cover class (shrublands). Here, the incidence angles vary across the entire possible range, from 30° to 50°, and the terrain heights are lowest, which leads to dominant soil scattering components instead of dominant volume scattering contributions (Figure 5A). At the monitoring site MOISST, dihedral scattering is dominant in the eastern part around the city *Stillwater* (Figure 5B), where the land is predominantly covered by grassland/herbaceous and smaller evergreen forests (Figure 2, Section 2). In contrast, regions mainly characterized by cultivated crops show dominant volume scattering, e.g., in the center of the site. Again, the results are influenced by the varying incidence angles, for instance, in the center of the site, where higher incidence angles lead to rather dominant soil scattering (Figure 5B). Lastly, Harvard Forest shows primarily dihedral scattering with only some regions in the northern part of the monitoring site, where soil or volume scattering are dominant (Figure 5C).

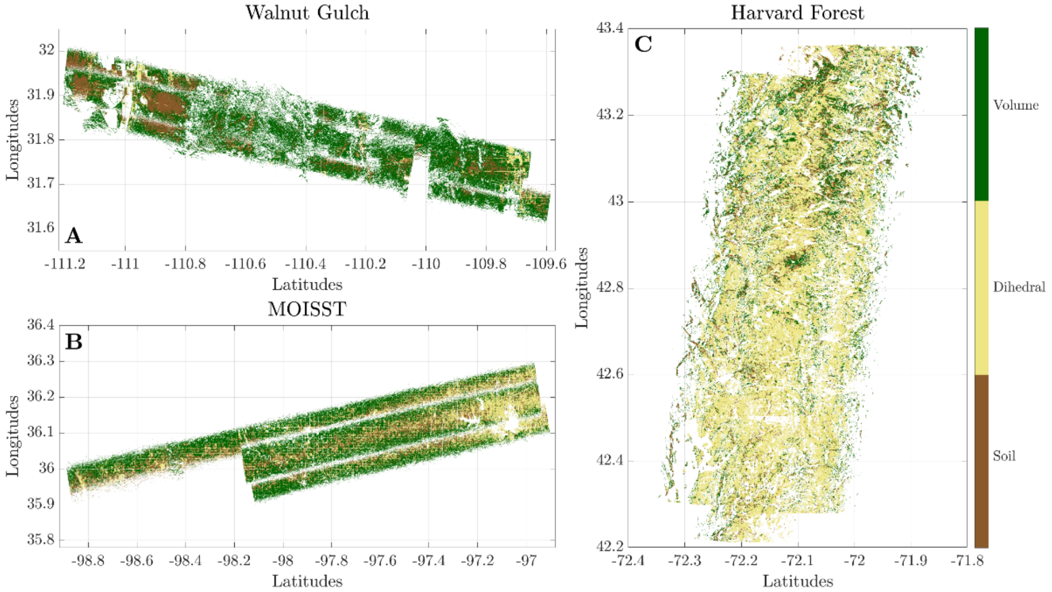

Figure 5. Estimated normalized, relative power indices representing dominant soil (P_s/P_t), dihedral (P_d/P_t), or volume (P_v/P_t) scattering at the AirMOSS monitoring sites. The average values of the most dominant scattering mechanism of all dates are displayed (Figure 1, Section 2). White data gaps originate from initial filtering of the input parameters. (**A**) Walnut Gulch, AZ, USA. (**B**) MOISST, OK, USA. (**C**) Harvard Forest, MA, USA.

For a comparison of all decomposition results for varying years, Figure 6 displays the average probability distribution function (PDF) of the normalized scattering contributions at each monitoring site. It can be seen that the PDF for soil scattering peaks at the lowest value but with the highest probability at Harvard Forest, while at Walnut Gulch and MOISST the normalized soil scattering is located between dihedral and volume scattering as second dominant scattering contribution, respectively (Figure 6, first row).

The dihedral scattering contribution is lowest at Walnut Gulch and MOISST but highest at Harvard Forest (Figure 6, second row), while the volume scattering contribution is highest at Walnut Gulch but lowest at Harvard Forest, with MOISST in between (Figure 6, third row). Moreover, there are hardly any differences in the estimated PDFs of all three relative indices between the years 2013 and 2015. Only the PDF for soil scattering contribution at Harvard Forest slightly decreases from 2013 to 2015, whereas the PDF for dihedral and volume scattering slightly increases (Figure 6, right column).

In summary, the monitoring site mainly covered by shrub/scrub (Walnut Gulch) displays the lowest dihedral and the highest volume scattering, while the monitoring site covered by forests (Harvard Forest) displays almost exclusively dihedral and the lowest vegetation scattering. The mixed monitoring site covered by grassland/herbaceous or cultivated crops (MOISST) shows almost balanced contributions of soil or volume scattering with dihedral scattering being predominant in regions of grassland/herbaceous and volume scattering in regions with extensive agriculture.

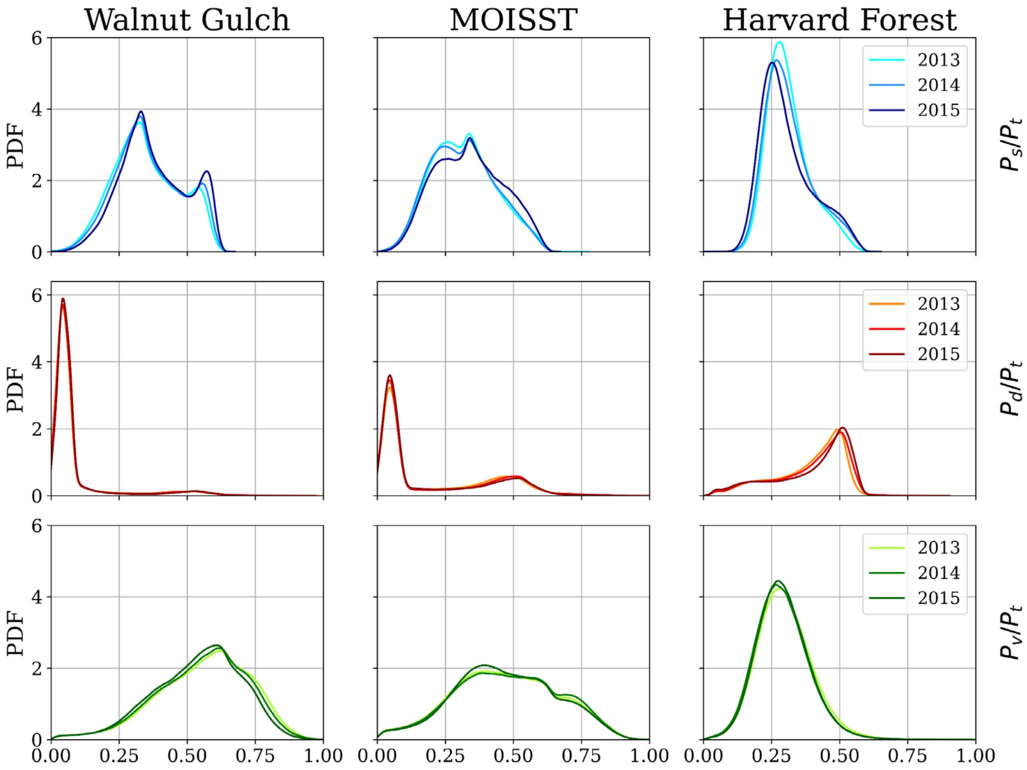

Figure 6. Probability density functions (PDFs) of estimated normalized, relative power indices representing soil (P_s/P_t; first row), dihedral (P_d/P_t; second row), or volume (P_v/P_t, third row) scattering at the AirMOSS monitoring sites. The average values of all four dates per year are shown (Figure 1, Section 2). Left column: Walnut Gulch, AZ, USA. Middle column: MOISST, OK, USA. Right column: Harvard Forest, MA, USA.

4.2. Results for Complex Soil Permittivity and P-Band Penetration Depth

In Figure 7, the real ε_s' and imaginary ε_s'' part of the estimated complex soil permittivity ε_s, determined with the proposed P-band SAR moisture estimation method (cf. Section 3.3), are displayed for the main land cover classes for each monitoring site and date (Table 1).

Walnut Gulch, covered by shrub/scrub (cf. Section 2), shows the overall lowest permittivity results with a median value of $\varepsilon_S = 11.2 - j1.5$. At the monitoring site MOISST, the main land cover class grassland/herbaceous shows slightly higher permittivity results with a median value of $\varepsilon_S = 14.9 - j1.7$. The latter is in contrast to the second dominant land cover class cultivated crops (cf. Section 2) with a median value of $\varepsilon_S = 13.8 - j1.5$. However, the results for cultivated crops span the largest value ranges of all classes and monitoring sites with the real part of permittivity varying from 6 to 31 and the imaginary part of permittivity varying from 1 to 3.2. The three main land cover classes, deciduous, mixed, and evergreen forest (cf. Section 2), at Harvard Forest display the overall smallest value ranges and the highest permittivity results with comparable median values of $\sim\varepsilon_S = 16 - j1.8$. Hence, the forest site Harvard Forest, characterized by a cold humid continental climate (cf. Section 2), shows the highest permittivity with the smallest deviations, while the driest monitoring site, mainly covered by shrub/scrub due to the arid climate (Walnut Gulch), shows the lowest permittivity results. The monitoring site characterized by a temperate climate and grassland/herbaceous or cultivated crops (MOISST) displays permittivity results in between.

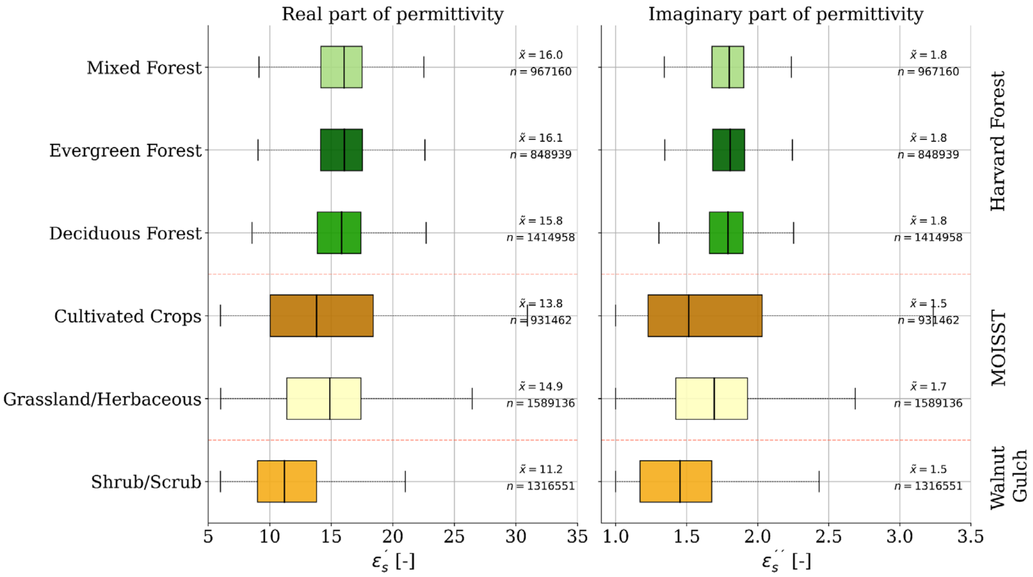

Figure 7. Estimated real ε_s' (**left**) and imaginary ε_s'' (**right**) part of complex soil permittivity for main land cover classes of the AirMOSS monitoring sites Walnut Gulch, MOISST, and Harvard Forest. The results are displayed for all acquisition dates (Figure 1, Section 2). $\tilde{x}$ represents the respective median value, n is the total amount of values per boxplot.

Converted to soil moisture, Walnut Gulch revealed values in a range from 12.6 vol.% to 34 vol.% with a median value of 18.8 vol.%. At MOISST, values ranged from 12.6 vol.% to 47.5 vol.% with a median value of 27.5 vol.%, and at Harvard Forest from 25.6 vol.% to 32.6 vol.% with a median value of 29.3 vol.%.

Based on the complex permittivity results, the penetration depth δ_P for each monitoring site is estimated according to Equation (20) (cf. Section 3.3). In Figure 8, areal results for δ_P are displayed for every AirMOSS monitoring site. At all sites, δ_P varies in comparable ranges from 5.7 cm, 5.4 cm, or 7.7 cm to 35 cm, with the majority of values from 20 cm to 35 cm. Walnut Gulch and MOISST show higher variations in results according to varying land cover classes, for instance, lower depths in regions where grassland/herbaceous or forests are dominant, and greater depths where shrublands or cultivated crops are dominant (Figure 2, Section 2). In contrast, at Harvard Forest only small deviations in results are observed with the majority of δ_P values being at around 25 cm. The two slightly apparent vertical stripes in the results with overall higher δ_P values originate from varying incidence angles of the sensing system across the monitoring site (Figure 8C).

In detail, variations in δ_P are largest, where land cover is rather heterogeneous. For instance, the monitoring site Harvard Forest, which is almost fully covered by forests (Figure 2, Section 2), displays the smallest deviations in results and a homogeneous map of δ_P across the entire site (Figure 8C). In contrast, in the eastern part of the monitoring site Walnut Gulch around the city *Elfrida*, highest variations in δ_P are estimated because in that region the land cover is a rather heterogeneous mixture of cultivated crops, grassland/herbaceous, and shrub/scrub. Further, in the center of the site Walnut Gulch at the *Whetstone Mountains*, which are covered by forests, the estimated δ_P are lower than in the surrounding areas, where shrub/scrub is dominant (Figure 2, Section 2). In the western part of Walnut Gulch, at the dip east of the *Green Valley* (Figure 2, Section 2), δ_P are lowest (Figure 8A).

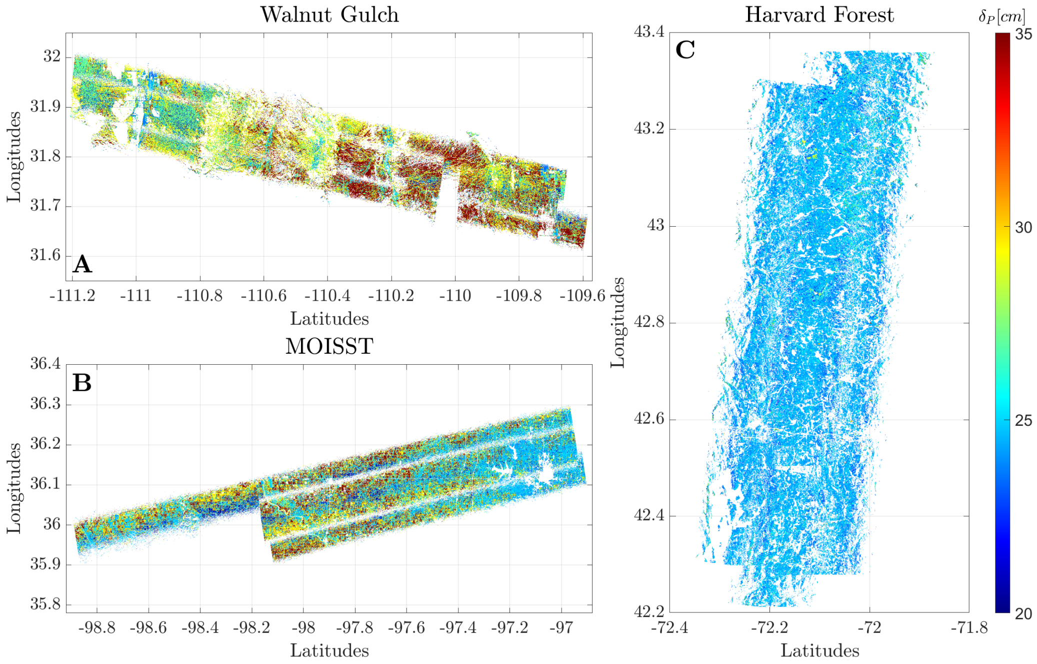

Figure 8. Estimated permittivity-based penetration depth δ_P at the AirMOSS monitoring sites. The average values of penetration depths of all dates are displayed (Figure 1, Section 2). White data gaps originate from initial filtering of the input parameters. (**A**) Walnut Gulch, AZ, USA. (**B**) MOISST, OK, USA. (**C**) Harvard Forest, MA, USA.

For detailed analyses, δ_P results are displayed in Figure 9 for the main land cover classes of the three monitoring sites. As can be seen in the upper plot of Figure 9, the land cover classes for forests (deciduous, evergreen, and mixed) at Harvard Forest have the lowest δ_P values of all landcover classes at ~24.6 cm, with the smallest variations in results, varying from ~22.8 cm to ~26.4 cm only. In contrast, at Walnut Gulch the highest median δ_P value is estimated at 27 cm, varying in the range from 16.8 to 35 cm. The results at the monitoring site MOISST display a median δ_P of 25.1 cm for grasslands/herbaceous and 25.7 cm for cultivated crops with the largest deviations in the latter land cover class (varying from 13.6 to 35 cm). Accordingly, PDFs in the lower plot of Figure 9 display the highest densities with the narrowest distributions for forest land cover classes, peaking from 24 to 25 cm, while other land cover classes reveal more distributed results, covering a broader range of δ_P estimates at lower densities (Figure 9).

4.3. Comparison of Permittivity Estimates with In Situ Measurements

For a comparison of the estimated soil permittivity with in situ soil moisture measurements at single locations (cf. Section 2), the results for ε'_s are converted to soil moisture θ [vol.%] according to the dielectric mixing model of [71].

In Figure 10, retrieved θ, based on the proposed P-band SAR moisture estimation method and P-band SAR measurements, are compared with in situ measured θ at the driest AirMOSS site, Walnut Gulch in Arizona. While retrieved values are in the range from 12.6 vol.% to 34 vol.% with a highest PDF from 12.5 vol.% to 19 vol.%, in situ measurements vary from 2.6 vol.% to 15.4 vol.% with the PDF peaking at 6.7 vol.%. Conducted statistical tests between retrieved and in situ measured θ values with a correlation coefficient (R^2) [–] and medium root-mean square error (RMSE) [vol.%] of $R^2 = 0.2$ and $RMSE = 14.1$ vol.% confirm a clear overestimation of retrieved θ compared to in situ measurements. The main reason for the low correlation could be the discrepancy between measuring depths since available in situ values are measured near the soil surface at ~0–5 cm, while for retrieved θ, based on decomposed P-band SAR observations, penetration depths proved to vary from 16.8 cm to 35 cm with median δ_P at 27 cm (Figure 9).

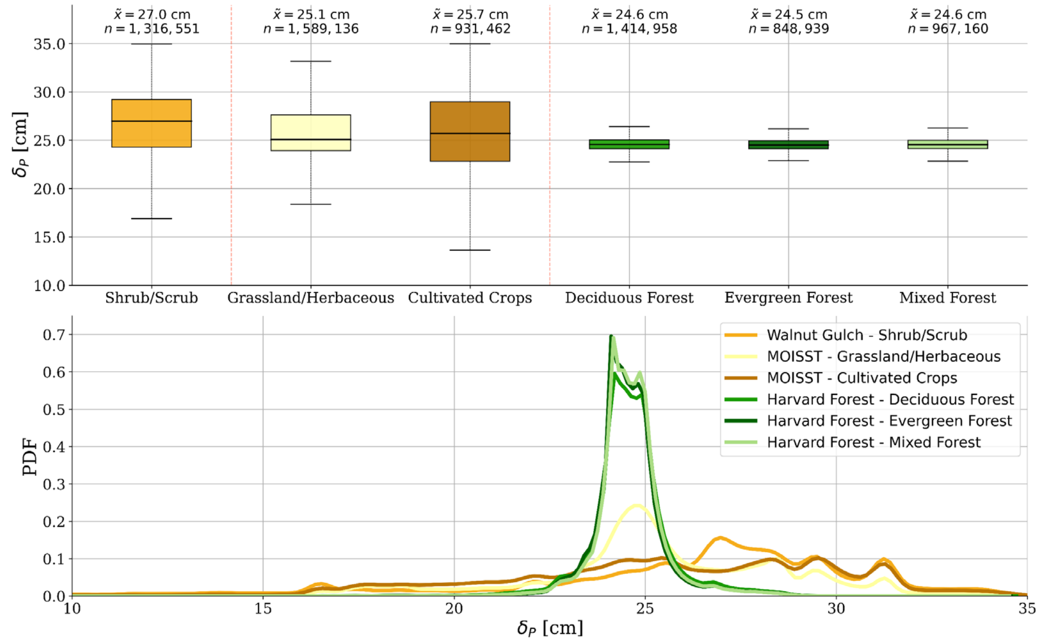

Figure 9. Boxplots and probability density functions (PDFs) of estimated permittivity-based penetration depths δ_P for main land cover classes at the AirMOSS monitoring sites Walnut Gulch, MOISST, and Harvard Forest. The results are displayed for all acquisition dates (Figure 1, Section 2). $\tilde{x}$ represents the respective median value, n is the total amount of values per boxplot.

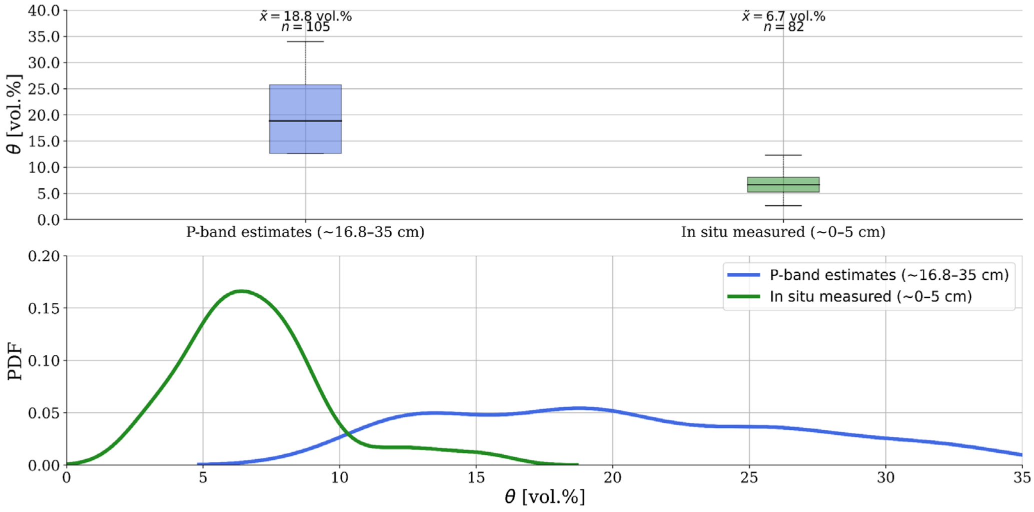

Figure 10. Comparison of retrieved soil moisture values, estimated with the proposed P-band SAR method and converted from permittivity according to the dielectric mixing model from [71], with in situ measured soil moisture values from various networks (cf. Section 2) at the AirMOSS monitoring site Walnut Gulch, AZ. $\tilde{x}$ represents the respective median value, n is the total amount of values per boxplot.

In Figure 11, the comparison is shown for the AirMOSS test site Harvard Forest. While retrieved θ vary in the range from 25.6 vol.% to 32.6 vol.%, with the PDF peaking at 29.3 vol.%, in situ measurements vary from 25.6 vol.% and 38.8 vol.%, with a median value of 32.4 vol.%.

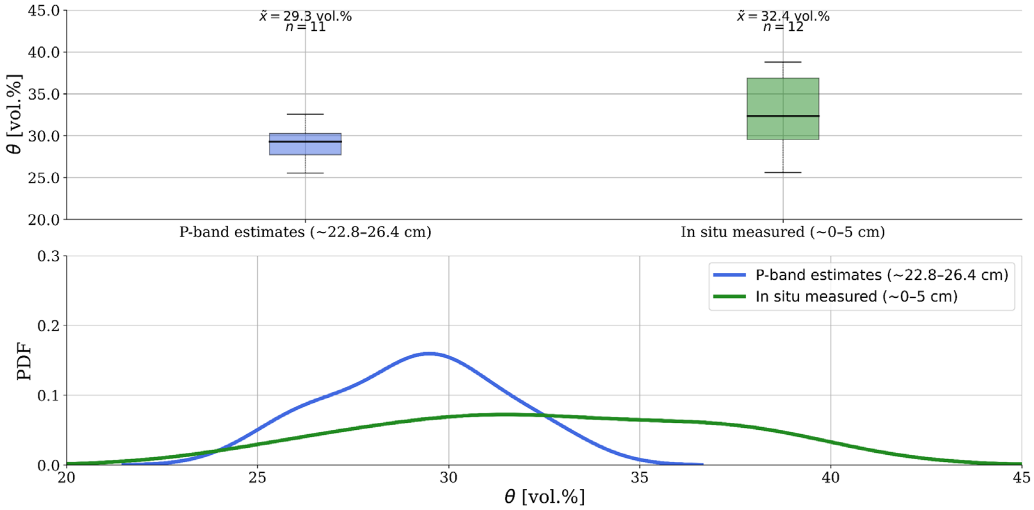

Figure 11. Comparison of retrieved soil moisture values, estimated with the proposed P-band SAR method and converted from permittivity according to the dielectric mixing model from [71], with in situ measured soil moisture values from various networks (cf. Section 2) at the AirMOSS monitoring site Harvard Forest, MA. $\tilde{x}$ represents the respective median value, n is the total amount of values per boxplot.

Hence, with estimated $R^2 = 0.5$ and $RMSE = 4.6$ vol.%, results show that the humid forest site displays a higher correlation and lower error between retrievals and in situ measurements compared to the arid site Walnut Gulch (Figure 10), despite the same discrepancy between measuring depths. In situ measurements are again only available from the soil surface at ~0–5 cm, while retrieval results showed average penetration depths around 24.6 cm, overall varying from 22.8 to 26.4 cm (Figure 9).

Lastly, the comparison of θ values is conducted for MOISST (Figure 12). Only for this site, in situ measurements for comparisons are available from the soil surface (~0–5 cm) and also for greater soil depths at ~5–10 cm and ~10–20 cm. The median values of in situ measured θ are increasing with greater measuring depths, from 16.4 vol.% near the soil surface to 24 vol.% at a soil depth of ~10–20 cm. Concurrently, the in situ value ranges are decreasing with greater soil depths, displaying the smallest deviations in measurements at a depth of ~10–20 cm, varying from 19.3 vol.% to 32.3 vol.%. In comparison, retrieved θ vary between 12.6 vol.% and 47.5 vol.% with a median value of 26.4 vol.%. Conducted statistics show $R^2 = 0.09$ and $RMSE = 13.5$ vol.% for 0–5 cm, $R^2 = 0.13$ and $RMSE = 12$ vol.% for 5–10 cm, and $R^2 = 0.09$ and $RMSE = 12.2$ vol.% for 10–20 cm. Hence, retrieval results correlate slightly worse with in situ measurements from the top-soil at ~0–5 cm compared to other measuring depths, and display the smallest difference in median values of ~2.4 vol.% with in situ measurements at the greatest measuring depth (~10–20 cm). However, estimated θ at MOISST showed a median penetration depth of 25.7 cm, with most values varying from 13.6 to 35 cm for landcover class cultivated crops (Figure 9). Hence, there is still a discrepancy between measuring depths, which explains a remaining difference between in situ (10–20 cm) and SAR-based soil moisture estimates.

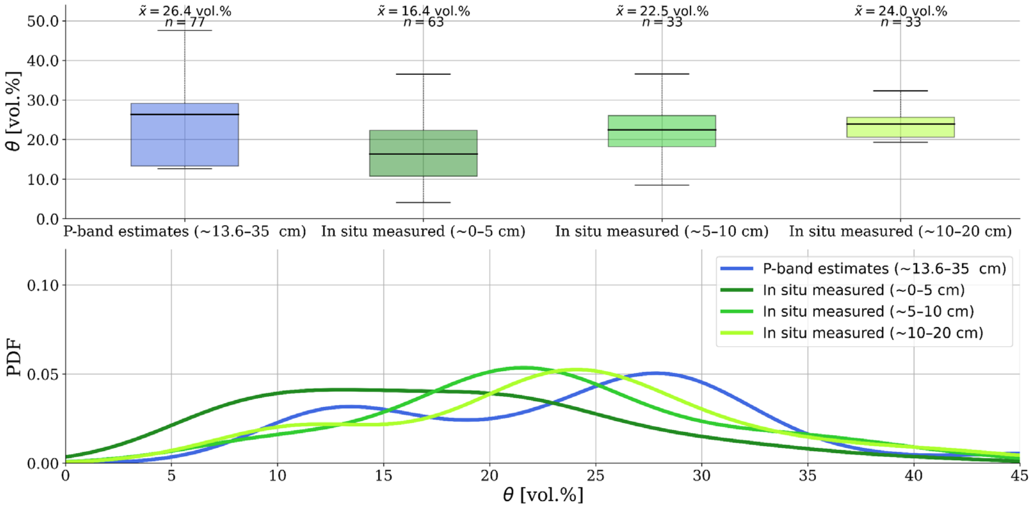

Figure 12. Comparison of retrieved soil moisture values, estimated with the proposed P-band SAR method and converted from permittivity according to the dielectric mixing model from [71], with in situ measured soil moisture values from various networks (cf. Section 2) at the AirMOSS monitoring site MOISST, OK. $\tilde{x}$ represents the respective median value, n is the total amount of values per boxplot.

5. Discussion

In comparison to model- or eigen-based decomposition methods, the hybrid decomposition technique proposed in this study combines both methods and further employs a soil scattering model suitable for P-band. Hence, the proposed P-band SAR moisture estimation method continues the efforts of [24], an iterative approach for soil moisture estimation applied to L-band observations, and of [3], the first hybrid decomposition method applied to P-band SAR data by assuming volume scattering as a cloud of randomly oriented dipoles (cf. Sections 1 and 3.2). Furthermore, the method proposed here is non-iterative with reduced algorithm complexity and, hence, computationally less expensive. It needs no prior assumptions on initial vegetation conditions since it allows the application of a wide range of vegetation cover characteristics in comparison to [3]. Lastly, it is the first of its kind, to the best of our knowledge, for complex soil permittivity estimation from (P-band) SAR data. The well-known problem of decomposition methods to overestimate the volume scattering components (cf. Section 1), e.g., [9,27,33], is solved by excluding any vegetation characterization from further analyses, where scattering intensities become negative (cf. Section 3.2). However, this is only feasible since multiple vegetation characterizations can be considered.

By applying the proposed P-band SAR moisture estimation method to SAR observations at three AirMOSS monitoring sites with varying land cover classes, the scattering contributions of surface, dihedral, or volume mechanisms could be estimated. Results show dominant dihedral scattering over forests at the site Harvard Forest in Massachusetts, and dominant volume scattering over shrub/scrub at the site Walnut Gulch in Arizona as well as over cultivated crops at the site MOISST in Oklahoma. Further, it is interesting to notice that cultivated crops at Walnut Gulch in Arizona show dominant dihedral scattering while cultivated crops at MOISST in Oklahoma display dominant volume scattering (Figure 5). This may be due to the different types and phenological stages of cultivated vegetation. Hence, results in this study suggest dominant dihedral scattering for increasing vegetation volume (height, density) at P-band. These results concur with previous studies. For example, [77] found strong dihedral scattering for P-band measurements across a boreal forest in Canada. They concluded that at P-band the ground and trunks contribute with more relevance to the SAR signal than the branches and leaves, since with “smaller scatterers compared to the wavelength” [77], these layers become more transparent to the incident wave compared to higher frequencies such as L- or C-band. This is supported by findings of [19] across the AirMOSS monitoring site MOISST, where results also demonstrated that vegetation is more transparent at P-band than at L-band, and that woody vegetation is needed for dihedral scattering to appear in P-band. Similarly, Ref. [78] estimated dominant dihedral scattering contributions due to mainly trunk–ground interactions in P-band SAR signals across eucalyptus species in woodlands on the east coast of Australia. Analogue results at L- or C-band, however, revealed predominant volume scattering from branches and leaves (C-band) or a mix of dihedral and volume scattering, depending on the polarization (L-band). They concluded that with multiple frequencies and polarizations, individual subsets of forest structures could be analyzed [78]. In contrast, findings from [3], which are based on the same AirMOSS dataset employed in this study, showed increasing volume scattering with increasing vegetation. In the case of the monitoring site Harvard Forest, they found mainly volume scattering and less dihedral scattering, contrary to the results presented. One reason may be that the applied method in [3] only considers one type of vegetation (randomly oriented dipoles) across the entire study area, and did not employ any soil scattering model for the determination of the volume intensity component prior to the decomposition of SAR signals. However, the results in this study are supported by the fact that overall lower penetration depths into the soil could be estimated across forests compared to shrub/scrub (Figure 9, Section 4.2.). Over forests, such as at Harvard Forest, P-band microwaves are able to penetrate through vegetation but less into soils, and interact more with trunks. In smaller and less densely vegetated areas such as shrub/scrub at Walnut Gulch, P-band microwaves are able to penetrate deeper into soils but interact more with present branches and leaves due to the absence of trunks (2nd scattering center for dihedral scattering), and thus display a higher volume scattering contribution in contrast to forests. Hence, the characterization of vegetation types within the decomposition method should be carefully addressed. Choosing only one type of representative will likely lead to a biased estimation of volume scattering in P-band SAR signals.

Based on the best fit between simulations and decomposition results, the complex soil permittivity was estimated. Analyses concur with the investigated land cover classes and the climatic circumstances at each monitoring site. Lowest soil permittivity was estimated across shrub/scrub in the hot deserts of Arizona, while the highest permittivity with the smallest deviations in results was determined over forests in Massachusetts, characterized by cold humid continental climates. Accordingly, results at the monitoring site in Oklahoma with a temperate climate displayed soil permittivity in between the former ranges. Lastly, the smallest deviations in results are found in the forest land cover classes, while the largest deviations in results are found for pixels classified as cultivated crops. This fits varying phenological stages of different vegetation types and irrigation situations on agricultural managed lands (Figure 7, Section 4.2).

Converted permittivity to soil moisture was then compared at single locations with in situ measurements. Unfortunately, in situ soil moisture values mainly of the top-soil layer (0–5 cm) are available for comparison, while P-band SAR penetration depth estimates indicate deeper penetration into the soil (mainly around 20–30 cm). Thus, the highest correlation with the lowest deviations was found at Harvard Forest, and the lowest correlations at MOISST, but with slightly increasing correlations for measurements at greater soil depths. Overall, correlations are low and RMSEs are high. The main reason for this is the discrepancy between sensing depths. While in situ soil moisture values are mainly measured near the soil surface at ~0–5 cm, the estimated soil moisture is based on P-band SAR observations, which proved to have penetration depths mainly from 20 cm to 35 cm. Thus, retrievals correlate less with near-surface soil moisture measurements but will more likely correlate with measurements at deeper soil depths, as indicated at MOISST (Figure 12, Section 4.3). At Walnut Gulch, for instance, retrievals are clearly overestimating in situ measurements, showing the highest error (cf. Section 4.3). Several studies revealed increasing soil moisture with greater soil depth until a certain point, e.g., [51,79–81]. For example, [80] showed increasing soil moisture values with increasing soil depth from 5 cm to 30 cm at Kendall, Arizona (Figure 2, Section 2). Further, in hot desert regions such as

Walnut Gulch, the soil surface layer as a land–atmosphere boundary is highly influenced by climate and weather conditions and, hence, the surface tends to dry out faster than the soil layers below [79]. Another source for error is the spatial discrepancy between field measurements and SAR-based observations. While the in situ measurements are point values from single locations (cf. Figure 2, Section 2), the estimated results based on the AirMOSS dataset have a spatial resolution of ~100 m.

Based on the estimated complex soil permittivity, permittivity-based penetration depths were calculated, leading to overall P-band depths from 5 to 35 cm. Highest variations occur in regions, where the land cover is rather heterogeneous or where influences of different phenological stages of the vegetation or irrigation situations lead to varying permittivity estimates. In detail, at the humid forest site the smallest penetration depths at a median value of 24.5 cm with the smallest deviations in results were estimated. Correspondingly, the driest monitoring site shows the greatest variations in penetration depths over cultivated crops, varying mainly from 16.8 to 35 cm around a median value of 27 cm. This is in accordance with previous studies. The authors of [40] showed that P-band can provide soil moisture retrievals for a depth greater than 10 cm when using a frequency lower than 0.5 GHz, while [46] estimated similar P-band penetration depths, varying from 15 to 36 cm, showing significant annual seasonality depending on the soil moisture content.

Lastly, following the assumption of [52], P-band penetration depths between 6.97 and 34.86 cm are realistic (cf. Section 1), which is almost exactly the value range estimated in this study (5 to 35 cm). Hence, depending on soil permittivity and vegetation cover characteristics, P-band is able to penetrate several decimeters into the soil, enabling the estimation of RZSM.

6. Conclusions and Outlook

In this study, a method for complex soil permittivity and permittivity-based penetration depth estimation based on P-band SAR data is proposed and implemented. For that, a hybrid decomposition technique is set up for separating fully polarimetric P-band SAR observations into individual scattering mechanisms (soil, dihedral, volume).

The proposed method extracts the soil scattering component by applying a hybrid (eigen- and model-based) decomposition method and incorporating a soil scattering model suitable for P-band frequency, the multi-layer SPM. To the best of our knowledge, this method is the first of its kind for complex soil permittivity estimation from P-band SAR data. The approach is only limited to fully polarimetric SAR observations as co- and cross-polarized coherency matrix elements are needed within the decomposition. Further, although the proposed approach provides the ability to consider many different types of vegetation structures, the characterization of varying vegetation types within the hybrid decomposition method should be carefully addressed.

Comparisons of retrieved soil moisture with in situ measurements show lower to medium correlations, proving the overall larger penetration of P-band microwaves into soils, since results match less with top-soil layer measurements but more with deeper (~20 cm) measurements. The lack of possibility to analyze retrieval results, presented in this study, with comparable soil moisture measurements, originating at least from similar soil depths, proves the need for measurements at greater soil depths. Overall, P-band penetration depths from 5 to 35 cm were estimated, depending on regional climate and land cover characteristics and heterogeneity.

In summary, the proposed method was further adapted and revised in order to overcome many drawbacks of previous decomposition methods (e.g., overestimation of volume scattering component, consideration of one single vegetation type, missing multi-layer structures for soil scattering at P-band), and to be applicable for complex soil permittivity estimation. Presented decomposition and complex permittivity results agree well with climate and soil conditions at the three different monitoring sites, proving the feasibility of the method. Further, estimated P-band penetration depths are in accordance with previous studies and confirm the overall higher penetration ability of P-band compared to L-band microwaves. In addition, strong dihedral scattering contributions in the SAR signal at P-band over forests, as shown in Figure 8 (cf. Section 4.2), are encouraging the development of an approach for soil moisture estimation under forests based on the dihedral scattering component instead of the soil scattering component, as proposed by [82].

Finally, since the proposed method only needs fully polarimetric P-band SAR measurements, it can be used to estimate complex soil permittivity and potential P-band penetration depths from space based on the SAR data of the upcoming BIOMASS mission (cf. Section 1) [13].

Author Contributions: Conceptualization, A.F. and T.J.; methodology, A.F. and T.J.; software, A.F.; validation, A.F. and T.J.; formal analysis, A.F. and T.J.; investigation, A.F. and T.J.; resources, A.F., A.T. and H.A.; data curation, A.F., H.A. and P.F.; writing—original draft preparation, A.F.; writing—review and editing, all authors; visualization, A.F.; supervision, T.J.; project administration, A.F., T.J., C.M. and E.F.; funding acquisition, T.J. and C.M. All authors have read and agreed to the published version of the manuscript.

Funding: This research was funded by the German Federal Ministry for Economic Affairs and Energy (BMWi) through the German Aerospace Center within the AssimEO project (50EE1914A).

Data Availability Statement: Not applicable.

Acknowledgments: A.F. and T.J. would like to thank colleagues from the Earth Observation Center at the German Aerospace Center for processing the data on a high-performance computing (HPC) cluster at the Leibniz Supercomputing Center (LRZ) as part of the high-performance data analytics (HPDA) terabyte project.

Conflicts of Interest: The authors declare no conflict of interest.

References

1. GCOS Status of the Global Observing System for Climate, GCOS Report No. 195. 2015. Available online: https://library.wmo.int/index.php?lvl=notice_display&id=18962 (accessed on 16 March 2021).
2. Bojinski, S.; Verstraete, M.; Peterson, T.C.; Richter, C.; Simmons, A.; Zemp, M. The Concept of Essential Climate Variables in Support of Climate Research, Applications, and Policy. *Bull. Am. Meteorol. Soc.* **2014**, *95*, 1431–1443. [CrossRef]
3. Alemohammad, S.H.; Konings, A.G.; Jagdhuber, T.; Moghaddam, M.; Entekhabi, D. Characterization of Vegetation and Soil Scattering Mechanisms across Different Biomes Using P-Band SAR Polarimetry. *Remote Sens. Environ.* **2018**, *209*, 107–117. [CrossRef]
4. Babaeian, E.; Sadeghi, M.; Jones, S.B.; Montzka, C.; Vereecken, H.; Tuller, M. Ground, Proximal, and Satellite Remote Sensing of Soil Moisture. *Rev. Geophys.* **2019**, *57*, 530–616. [CrossRef]
5. Etminan, A.; Tabatabaeenejad, A.; Moghaddam, M. Retrieving Root-Zone Soil Moisture Profile From P-Band Radar via Hybrid Global and Local Optimization. *IEEE Trans. Geosci. Remote Sens.* **2020**, *58*, 5400–5408. [CrossRef]
6. Hoeben, R.; Troch, P.A. Assimilation of Active Microwave Observation Data for Soil Moisture Profile Estimation. *Water Resour. Res.* **2000**, *36*, 2805–2819. [CrossRef]
7. Truong-Loi, M.-L.; Saatchi, S.; Jaruwatanadilok, S. Soil Moisture Estimation Under Tropical Forests Using UHF Radar Polarimetry. *IEEE Trans. Geosci. Remote Sens.* **2015**, *53*, 1718–1727. [CrossRef]
8. Entekhabi, D.; Yueh, S.; De Lannoy, G. *SMAP Handbook*; NASA: Washington, DC, USA, 2014.
9. He, L.; Panciera, R.; Tanase, M.A.; Walker, J.P.; Qin, Q. Soil Moisture Retrieval in Agricultural Fields Using Adaptive Model-Based Polarimetric Decomposition of SAR Data. *IEEE Trans. Geosci. Remote Sens.* **2016**, *54*, 4445–4460. [CrossRef]
10. Kerr, Y.H.; Al-Yaari, A.; Rodriguez-Fernandez, N.; Parrens, M.; Molero, B.; Leroux, D.; Bircher, S.; Mahmoodi, A.; Mialon, A.; Richaume, P.; et al. Overview of SMOS Performance in Terms of Global Soil Moisture Monitoring after Six Years in Operation. *Remote Sens. Environ.* **2016**, *180*, 40–63. [CrossRef]
11. Ulaby, F.T.; Dubois, P.C.; van Zyl, J. Radar Mapping of Surface Soil Moisture. *J. Hydrol.* **1996**, *184*, 57–84. [CrossRef]
12. Wang, H.; Magagi, R.; Goita, K.; Jagdhuber, T.; Hajnsek, I. Evaluation of Simplified Polarimetric Decomposition for Soil Moisture Retrieval over Vegetated Agricultural Fields. *Remote Sens.* **2016**, *8*, 142. [CrossRef]
13. Gelas, C.; Villard, L.; Ferro-Famil, L.; Polidori, L.; Koleck, T.; Daniel, S. Multi-Temporal Speckle Filtering of Polarimetric P-Band SAR Data over Dense Tropical Forests: Study Case in French Guiana for the BIOMASS Mission. *Remote Sens.* **2021**, *13*, 142. [CrossRef]
14. Garrison, J.L.; Shah, R.; Kim, S.; Piepmeier, J.; Vega, M.A.; Spencer, D.A.; Banting, R.; Raymond, J.C.; Nold, B.; Larsen, K.; et al. Analyses Supporting SNoOPI: A P-Band Reflectrometry Demonstration. In Proceedings of the IGARSS 2020—2020 IEEE International Geoscience and Remote Sensing Symposium, Waikoloa, HI, USA, 26 September–2 October 2020; pp. 3349–3352.

15. NASA. 2019. Available online: https://www.nasa.gov/feature/goddard/2019/snoopi-a-flying-ace-for-soil-moisture-and-snow-measurements (accessed on 16 March 2021).
16. Chapin, E.; Chau, A.; Chen, J.; Heavey, B.; Hensley, S.; Lou, Y.; Machuzak, R.; Moghaddam, M. AirMOSS: An Airborne P-Band SAR to Measure Root-Zone Soil Moisture. In Proceedings of the 2012 IEEE Radar Conference, Atlanta, GA, USA, 7–11 May 2012; pp. 693–698.
17. Alberga, V.; Satalino, G.; Staykova, D.K. Comparison of Polarimetric SAR Observables in Terms of Classification Performance. *Int. J. Remote Sens.* **2008**, *29*, 4129–4150. [CrossRef]
18. Yamaguchi, Y.; Yajima, Y.; Yamada, H. A Four-Component Decomposition of POLSAR Images Based on the Coherency Matrix. *IEEE Geosci. Remote Sens. Lett.* **2006**, *3*, 292–296. [CrossRef]
19. Alemohammad, S.H.; Jagdhuber, T.; Moghaddam, M.; Entekhabi, D. Soil and Vegetation Scattering Contributions in L-Band and P-Band Polarimetric SAR Observations. *IEEE Trans. Geosci. Remote Sens.* **2019**, *57*, 8417–8429. [CrossRef]
20. Cloude, S.R. Uniqueness of Target Decomposition Theorems in Radar Polarimetry. In *Direct and Inverse Methods in Radar Polarimetry*; Boerner, W.-M., Brand, H., Cram, L.A., Holm, W.A., Stein, D.E., Wiesbeck, W., Keydel, W., Giuli, D., Gjessing, D.T., Molinet, F.A., Eds.; Springer: Dordrecht, The Netherlands, 1992; pp. 267–296; ISBN 978-94-010-9245-6.
21. Freeman, A.; Durden, S.L. A Three-Component Scattering Model for Polarimetric SAR Data. *IEEE Trans. Geosci. Remote Sens.* **1998**, *36*, 963–973. [CrossRef]
22. van Zyl, J.J.; Arii, M.; Kim, Y. Model-Based Decomposition of Polarimetric SAR Covariance Matrices Constrained for Nonnegative Eigenvalues. *IEEE Trans. Geosci. Remote Sens.* **2011**, *49*, 3452–3459. [CrossRef]
23. Yonezawa, C.; Watanabe, M.; Saito, G. Polarimetric Decomposition Analysis of ALOS PALSAR Observation Data before and after a Landslide Event. *Remote Sens.* **2012**, *4*, 2314–2328. [CrossRef]
24. Jagdhuber, T.; Hajnsek, I.; Papathanassiou, K.P. An Iterative Generalized Hybrid Decomposition for Soil Moisture Retrieval Under Vegetation Cover Using Fully Polarimetric SAR. *IEEE J. Sel. Top. Appl. Earth Obs. Remote Sens.* **2015**, *8*, 3911–3922. [CrossRef]
25. Ballester-Berman, J.D.; Ainsworth, T.L.; Lopez-Sanchez, J.M. On The Physical Quantitative Assessment of Model-Based PolSAR Decompositions. *arXiv* **2020**, arXiv:2001.05872.
26. Chen, S.-W.; Sato, M.; Wang, X.-S.; Xiao, S.-P. *Target Scattering Mechanism in Polarimetric Synthetic Aperture Radar: Interpretation and Application*, 1st ed.; Springer: Singapore, 2018; ISBN 978-981-10-7269-7.
27. Cloude, S. *Polarisation: Applications in Remote Sensing*, 1st ed.; Oxford University Press: Oxford, UK; New York, NY, USA, 2010; ISBN 978-0-19-956973-1.
28. Cloude, S.R.; Pottier, E. A Review of Target Decomposition Theorems in Radar Polarimetry. *IEEE Trans. Geosci. Remote Sens.* **1996**, *34*, 498–518. [CrossRef]
29. Hajnsek, I.; Desnos, Y.-L. *Polarimetric Synthetic Aperture Radar Principles and Application*; Springer: Berlin/Heidelberg, Germany, 2021; ISBN 978-3-030-56504-6.
30. Van Zyl, J.; Kim, Y. *Synthetic Aperture Radar Polarimetry*; JPL Space Science and Technology Series; Wiley: Hoboken, NJ, USA, 2011; ISBN 978-1-118-11607-4.
31. Jagdhuber, T. Soil Parameter Retrieval under Vegetation Cover Using SAR Polarimetry. Ph.D. Thesis, Faculty of Science, University Potsdam, Potsdam, Germany, 2012. Available online: https://publishup.uni-potsdam.de/frontdoor/index/index/docId/5894 (accessed on 18 February 2021).
32. Sato, A.; Yamaguchi, Y.; Singh, G.; Park, S.-E. Four-Component Scattering Power Decomposition With Extended Volume Scattering Model. *IEEE Geosci. Remote Sens. Lett.* **2012**, *9*, 166–170. [CrossRef]
33. van Zyl, J.J.; Kim, Y. Requirements for Model-Based Polarimetric Decompositions. In Proceedings of the 7th European Conference on Synthetic Aperture Radar, Friedrichshafen, Germany, 2–5 June 2008.
34. Kraus, J.D.; Carver, K.R. *Electromagnetics*, 2nd ed.; McGraw-Hill Electrical and Electronic Engineering Series; McGraw-Hill: New York, NY, USA, 1973; ISBN 978-0-07-035396-1.
35. Ulaby, F.T.; Long, D.G. *Microwave Radar and Radiometric Remote Sensing*; The University of Michigan Press: Ann Arbor, MI, USA, 2014; ISBN 978-0-472-11935-6.
36. Bannawat, L.; Boonpoonga, A.; Akkaraekthalin, P. Permittivity Estimation of a Shallow-Layered Medium Using High-Resolution Ground-Penetrating Radar. *Int. J. Remote Sens.* **2020**, *41*, 4626–4643. [CrossRef]
37. Gururaj, P.; Umesh, P.; Shetty, A. Assessment of Surface Soil Moisture from ALOS PALSAR-2 in Small-Scale Maize Fields Using Polarimetric Decomposition Technique. *Acta Geophys.* **2021**, *69*, 579–588. [CrossRef]
38. Shi, H.; Zhao, L.; Yang, J.; Lopez-Sanchez, J.M.; Zhao, J.; Sun, W.; Shi, L.; Li, P. Soil Moisture Retrieval over Agricultural Fields from L-Band Multi-Incidence and Multitemporal PolSAR Observations Using Polarimetric Decomposition Techniques. *Remote Sens. Environ.* **2021**, *261*, 112485. [CrossRef]
39. Chen, R.H.; Tabatabaeenejad, A.; Moghaddam, M. Retrieval of Permafrost Active Layer Properties Using Time-Series P-Band Radar Observations. *IEEE Trans. Geosci. Remote Sens.* **2019**, *57*, 6037–6054. [CrossRef]
40. Shen, X.; Walker, J.P.; Ye, N.; Wu, X.; Boopathi, N.; Yeo, I.-Y.; Zhang, L.; Zhu, L. Soil Moisture Retrieval Depth of P- and L-Band Radiometry: Predictions and Observations. *IEEE Trans. Geosci. Remote Sens.* **2020**, *59*, 6814–6822. [CrossRef]
41. Ulaby, F.T.; Moore, R.K.; Fung, A.K.; Ulaby, F.T. *Microwave Remote Sensing, Active and Passive, Vol. II: Radar Remote Sensing and Surface Scattering and Emission Theory*; ARTECH House: Norwood, MA, USA, 1982; Volume 2, ISBN 978-0-201-10760-9.

42. El Hajj, M.; Baghdadi, N.; Bazzi, H.; Zribi, M. Penetration Analysis of SAR Signals in the C and L Bands for Wheat, Maize, and Grasslands. *Remote Sens.* **2018**, *11*, 31. [CrossRef]
43. Klausing, H.; Holpp, W. *Radar Mit Realer Und Synthetischer Apertur: Konzeption und Realisierung*; Oldenbourg: München, Germany, 2000; ISBN 978-3-486-23475-6.
44. Schaber, G.; McCauley, J.; Breed, C.; Olhoeft, G. Shuttle Imaging Radar: Physical Controls on Signal Penetration and Subsurface Scattenng in the Eastern Sahara. *IEEE Trans. Geosci. Remote Sens.* **1986**, *GE-24*, 603–623. [CrossRef]
45. Wilheit, T.T. Radiative Transfer in a Plane Stratified Dielectric. *IEEE Trans. Geosci. Electron.* **1978**, *16*, 138–143. [CrossRef]
46. Konings, A.G.; Entekhabi, D.; Moghaddam, M.; Saatchi, S.S. The Effect of Variable Soil Moisture Profiles on P-Band Backscatter. *IEEE Trans. Geosci. Remote Sens.* **2014**, *52*, 6315–6325. [CrossRef]
47. Blumberg, D.G.; Freilikher, V.; Lyalko, I.V.; Vulfson, L.D.; Kotlyar, A.L.; Shevchenko, V.N.; Ryabokonenko, A.D. Soil Moisture (Water-Content) Assessment by an Airborne Scatterometer: The Chernobyl disaster area and the Negev Desert. *Remote Sens. Environ.* **2000**, *71*, 309–319. [CrossRef]
48. Zribi, M.; Sahnoun, M.; Baghdadi, N.; Le Toan, T.; Ben Hamida, A. Analysis of the Relationship between Backscattered P-Band Radar Signals and Soil Roughness. *Remote Sens. Environ.* **2016**, *186*, 13–21. [CrossRef]
49. Ochsner, T.E.; Cosh, M.H.; Cuenca, R.H.; Dorigo, W.A.; Draper, C.S.; Hagimoto, Y.; Kerr, Y.H.; Larson, K.M.; Njoku, E.G.; Small, E.E.; et al. State of the Art in Large-Scale Soil Moisture Monitoring. *Soil Sci. Soc. Am. J.* **2013**, *77*, 1888–1919. [CrossRef]
50. Singh, A.; Meena, G.K.; Kumar, S.; Gaurav, K. Analysis of the Effect of Incidence Angle and Moisture Content on the Penetration Depth of L- and S-Band SAR Signals into the Ground Surface. *ISPRS Ann. Photogramm. Remote Sens. Spat. Inf. Sci.* **2018**, *4*, 197–202. [CrossRef]
51. Tabatabaeenejad, A.; Chen, R.H.; Burgin, M.S.; Duan, X.; Cuenca, R.H.; Cosh, M.H.; Scott, R.L.; Moghaddam, M. Assessment and Validation of AirMOSS P-Band Root-Zone Soil Moisture Products. *IEEE Trans. Geosci. Remote Sens.* **2020**, *58*, 6181–6196. [CrossRef]
52. de Lange, R.; Beck, R.; van de Giesen, N.; Friesen, J.; de Wit, A.; Wagner, W. Scatterometer-Derived Soil Moisture Calibrated for Soil Texture With a One-Dimensional Water-Flow Model. *IEEE Trans. Geosci. Remote Sens.* **2008**, *46*, 4041–4049. [CrossRef]
53. Rao, K.S.; Chandra, G.; Narasimha Rao, P.V. Study on Penetration Depth and Its Dependence on Frequency, Soil Moisture, Texture and Temperature in the Context of Microwave Remote Sensing. *J Indian Soc. Remote Sens.* **1988**, *16*, 7–19. [CrossRef]
54. Moghaddam, M.; Tabatabaeenejad, A.; Chen, R.H.; Saatchi, S.; Jaruwatanadilok, S.; Burgin, M.; Duan, X.; Truong-Loi, M.L. *AirMOSS: L2/3 Volumetric Soil Moisture Profiles Derived from Radar, 2012–2015*; ORNL DAAC: Oak Ridge, TN, USA, 2016. [CrossRef]
55. Peel, M.C.; Finlayson, B.L.; McMahon, T.A. Updated World Map of the Köppen-Geiger Climate Classification. *Hydrol. Earth Syst. Sci.* **2007**, *11*, 1633–1644. [CrossRef]
56. Homer, C.; Dewitz, J.; Yang, L.; Jin, S.; Danielson, P.; Xian, G.; Coulston, J.; Herold, N.; Wickham, J.; Megown, K. Completion of the 2011 National Land Cover Database for the Conterminous United States-Representing a Decade of Land Cover Change Information. *Photogramm. Eng. Remote Sens.* **2015**, *81*, 345–354.
57. Pastorello, G.; Trotta, C.; Canfora, E.; Chu, H.; Christianson, D.; Cheah, Y.W.; Poindexter, C.; Chen, J.; Elbashandy, A.; Humphrey, M.; et al. The FLUXNET2015 Dataset and the ONEFlux Processing Pipeline for Eddy Covariance Data. *Sci. Data* **2020**, *7*, 225. [CrossRef]
58. Montzka, C.; Bogena, H.; Zreda, M.; Monerris, A.; Morrison, R.; Muddu, S.; Vereecken, H. Validation of Spaceborne and Modelled Surface Soil Moisture Products with Cosmic-Ray Neutron Probes. *Remote Sens.* **2017**, *9*, 103. [CrossRef]
59. Zreda, M.; Shuttleworth, W.J.; Zeng, X.; Zweck, C.; Desilets, D.; Franz, T.; Rosolem, R. COSMOS: The COsmic-Ray Soil Moisture Observing System. *Hydrol. Earth Syst. Sci.* **2012**, *16*, 4079–4099. [CrossRef]
60. Moghaddam, M.; Silva, A.; Clewley, D.; Akbar, R.; Hussaini, S.A.; Whitcomb, J.; Devarakonda, R.; Shrestha, R.; Cook, R.B.; Prakash, G.; et al. *Soil Moisture Profiles and Temperature Data from SoilSCAPE Sites, USA*; ORNL DAAC: Oak Ridge, TN, USA, 2016. [CrossRef]
61. Bell, J.E.; Palecki, M.A.; Baker, C.B.; Collins, W.G.; Lawrimore, J.H.; Leeper, R.D.; Hall, M.E.; Kochendorfer, J.; Meyers, T.P.; Wilson, T.; et al. U.S. Climate Reference Network Soil Moisture and Temperature Observations. *J. Hydrometeorol.* **2013**, *14*, 977–988. [CrossRef]
62. Larson, K.M.; Small, E.E.; Gutmann, E.D.; Bilich, A.L.; Braun, J.J.; Zavorotny, V.U. Use of GPS Receivers as a Soil Moisture Network for Water Cycle Studies. *Geophys. Res. Lett.* **2008**, *35*, L24405. [CrossRef]
63. Tabatabaeenejad, A.; Moghaddam, M. Bistatic Scattering from Three-Dimensional Layered Rough Surfaces. *IEEE Trans. Geosci. Remote Sens.* **2006**, *44*, 2102–2114. [CrossRef]
64. Tsang, L.; Kong, J.A.; Shin, R.T. *Theory of Microwave Remote Sensing*; Wiley Series in Remote Sensing; Wiley: New York, NY, USA, 1985; ISBN 978-0-471-88860-4.
65. Nicolaides, A. *Pure Mathematics: Complex Numbers*; P.A.S.S: London, UK, 2008; Volume 3, ISBN 978-1-872684-92-5.
66. Rizzoli, P.; Martone, M.; Gonzalez, C.; Wecklich, C.; Borla Tridon, D.; Bräutigam, B.; Bachmann, M.; Schulze, D.; Fritz, T.; Huber, M.; et al. Generation and Performance Assessment of the Global TanDEM-X Digital Elevation Model. *ISPRS J. Photogramm. Remote Sens.* **2017**, *132*, 119–139. [CrossRef]
67. GDAL/OGR contributors GDAL/OGR Geospatial Data Abstraction Software Library. Open Source Geospatial Foundation. 2021. Available online: https://Gdal.Org (accessed on 16 March 2021).

68. QGIS Development Team QGIS Geographic Information System. Open Source Geospatial Foundation Project. 2021. Available online: http://Qgis.Osgeo.Org (accessed on 16 March 2021).
69. Szigarski, C.; Jagdhuber, T.; Baur, M.; Thiel, C.; Parrens, M.; Wigneron, J.-P.; Piles, M.; Entekhabi, D. Analysis of the Radar Vegetation Index and Potential Improvements. *Remote Sens.* **2018**, *10*, 1776. [CrossRef]
70. Kelleners, T.J.; Robinson, D.A.; Shouse, P.J.; Ayars, J.E.; Skaggs, T.H. Frequency Dependence of the Complex Permittivity and Its Impact on Dielectric Sensor Calibration in Soils. *Soil Sci. Soc. Am. J.* **2005**, *69*, 67–76. [CrossRef]
71. Topp, G.C.; Davis, J.L.; Annan, A.P. Electromagnetic Determination of Soil Water Content: Measurements in Coaxial Transmission Lines. *Water Resour. Res.* **1980**, *16*, 574–582. [CrossRef]
72. Dobson, M.; Ulaby, F.; Hallikainen, M.; El-rayes, M. Microwave Dielectric Behavior of Wet Soil-Part II: Dielectric Mixing Models. *IEEE Trans. Geosci. Remote Sens.* **1985**, *GE-23*, 35–46. [CrossRef]
73. Mironov, V.L.; Kosolapova, L.G.; Fomin, S.V. Physically and Mineralogically Based Spectroscopic Dielectric Model for Moist Soils. *IEEE Trans. Geosci. Remote Sens.* **2009**, *47*, 2059–2070. [CrossRef]
74. Park, C.-H.; Behrendt, A.; LeDrew, E.; Wulfmeyer, V. New Approach for Calculating the Effective Dielectric Constant of the Moist Soil for Microwaves. *Remote Sens.* **2017**, *9*, 732. [CrossRef]
75. von Hippel, A.R. *Dielectrics and Waves*; Wiley: New York, NY, USA, 1954.
76. Mironov, V.L.; Dobson, M.C.; Kaupp, V.H.; Komarov, S.A.; Kleshchenko, V.N. Generalized Refractive Mixing Dielectric Model for Moist Soils. In Proceedings of the IEEE International Geoscience and Remote Sensing Symposium, Toronto, ON, Canada, 24–28 June 2002; Volume 6, pp. 3556–3558.
77. Moghaddam, M.; Saatchi, S. Analysis of Scattering Mechanisms in SAR Imagery over Boreal Forest: Results from BOREAS '93. *IEEE Trans. Geosci. Remote Sens.* **1995**, *33*, 1290–1296. [CrossRef]
78. Lucas, R.M.; Moghaddam, M.; Cronin, N. Microwave Scattering from Mixed-Species Forests, Queensland, Australia. *IEEE Trans. Geosci. Remote Sens.* **2004**, *42*, 2142–2159. [CrossRef]
79. Das, N.N.; Mohanty, B.P.; Cosh, M.H.; Jackson, T.J. Modeling and Assimilation of Root Zone Soil Moisture Using Remote Sensing Observations in Walnut Gulch Watershed during SMEX04. *Remote Sens. Environ.* **2008**, *112*, 415–429. [CrossRef]
80. Sivandran, G.; Bras, R.L. Dynamic Root Distributions in Ecohydrological Modeling: A Case Study at Walnut Gulch Experimental Watershed. *Water Resour. Res.* **2013**, *49*, 3292–3305. [CrossRef]
81. Tabatabaeenejad, A.; Burgin, M.; Duan, X.; Moghaddam, M. P-Band Radar Retrieval of Subsurface Soil Moisture Profile as a Second-Order Polynomial: First AirMOSS Results. *IEEE Trans. Geosci. Remote Sens.* **2015**, *53*, 645–658. [CrossRef]
82. Jagdhuber, T. An Approach to Extended Fresnel Scattering for Modeling of Depolarizing Soil-Trunk Double-Bounce Scattering. *Remote Sens.* **2016**, *8*, 818. [CrossRef]